nature portfolio

https://doi.org/10.1038/s41565-022-01105-4

Supplementary information

Performance descriptors of nanostructured metal catalysts for acetylene hydrochlorination

In the format provided by the authors and unedited

Supplementary Information

Performance descriptors of nanostructured metal catalysts for acetylene hydrochlorination

Selina K. Kaiser[1‡], Edvin Fako[2‡], Ivan Surin[1], Frank Krumeich[1], Vita A. Kondratenko[3], Evgenii V. Kondratenko[3], Adam H. Clark[4], Núria López[2]*, and Javier Pérez-Ramírez[1]*

[1] Institute for Chemical and Bioengineering, Department of Chemistry and Applied Biosciences, ETH Zurich, Vladimir-Prelog-Weg 1, 8093 Zurich, Switzerland.

[2] Institute of Chemical Research of Catalonia (ICIQ), The Barcelona Institute of Science and Technology, Av. Països Catalans 16, 43007 Tarragona, Spain.

[3] Leibniz-Institut für Katalyse e. V., Albert-Einstein-Straße 29a, 18059 Rostock, Germany.

[4] Paul Scherrer Institut, 5232 Villigen PSI, Switzerland.

[‡] These authors contributed equally.

* Corresponding authors. E-mails: nlopez@iciq.es, jpr@chem.ethz.ch

Table of Contents

(I) Platform of Nanostructured Catalysts

To assess potential catalytic descriptors, a well-defined catalyst platform with systematically varied properties is central. Herein, the metal speciation and host functionalization are the factors of major interest, as they were previously identified to affect the overall catalytic performance for Au, Pt, and Ru-based catalysts. Hence, similar sensitivities can be expected for other active metals, including Rh, Ir, and Pd. To study both variables, we constructed a platform of M/C catalysts containing the six metals (M) with different nanostructure, varying from single atoms (SA) to nanoparticles (NP) of gradually increasing size at a fixed metal loading, supported on activated and N-doped carbon (AC, NC, **Fig. 1a**). To this end, the carbon supports were impregnated with a solution of the metal chloride precursors, followed by thermal activation at distinct temperatures (T_{act}, for details on the sample nomenclature, see **Supplementary Table 1**). By combining currently available state-of-the-art characterization techniques to analyse metal nuclearity and speciation in powder catalysts, including aberration corrected high-angle annular dark-field (AC-HAADF) STEM, X-ray diffraction (XRD), XAS, XPS, and DFT the evolution of the metal site as a function of the choice of metal, the thermal activation temperature, and the functionalization of the carbon support, was assessed. At T_{act} = 473 K, all metals are exclusively present as single atoms, as visualized by STEM analysis (**Fig. 1b**, **Supplementary Figs. 1**, **2**) and corroborated by the absence of respective metal reflections in the XRD patterns (**Supplementary Fig. 3**). XPS and extended X-ray absorption fine structure (EXAFS) fitting results indicate a positively charged metal center with *ca.* 2-4 chlorine neighboring atoms and the absence of metal-metal fingerprints in all cases (**Fig. 1c**, **Supplementary Figs. 4-9**, **Supplementary Tables 2-5**). Notably, the partially or fully chlorinated state of the metals largely impairs their ability to adsorb common probe molecules, such as carbon monoxide, thus disqualifying probe molecule vibrational spectroscopy as a tool to further characterize the SACs reported in this work. Despite the common initial speciation patterns (*i.e.*, isolated atoms), an increase in the thermal activation temperature triggers distinct behaviors for all metals, depending on the choice of carbon host. On AC, the population of metal chloride single atoms is systematically decreased with rising temperature due to gradual agglomeration into nanoparticles with small average particle sizes for Pt, Ru,

Rh, and Ir (d_p = 3-5 nm at T_{act} = 1073 K) and larger sizes for Au and Pd (d_p = 7.1 nm for Au at T_{act} = 523 K and d_p = 11.3 nm for Pd at T_{act} = 673 K, **Supplementary Fig. 1**). Based on XPS and EXAFS analyses, the nature of the obtained nanoparticles was identified as mainly metallic, in the case of Au, Pt, and Pd, and oxidic for Ru, Rh, and Ir. Notably, on NC, the former group does not undergo agglomeration with increasing thermal activation up to 1073 K. Instead, a gradual change in the coordination environment from predominantly M-Cl_x single atoms to M-N_4 single atoms occurs (*i.e.*, coordinated to 4 nitrogen neighboring atoms). On the contrary, the agglomeration behavior of Ru, Rh, and Ir is hardly affected by the choice of the carbon host and small metal oxide particles are formed with increasing activation temperature.

To rationalize the transformation of the metal speciation in the M/C catalysts during the catalyst synthesis, three aspects were considered: (*i*) the metal cohesive energy, E_{coh}, indicating the stability of the bulk metal, (*ii*) the metal oxide formation energy, E_{form}(M-oxide), describing the stability of the metal oxide, and (*iii*) the single-atom formation energies in their most stable configurations in chlorinated and non-chlorinated form, E_{form}(MCl) and E_{form}(SA), quantifying the interaction strength of single atoms to the surface defects of the carbon (N-defects on NC and O-defects on AC, respectively). Considering the former two, it is evident that E_{coh} and E_{form}(M-oxide) are linearly dependent (**Fig. 2a**). This implies that the origin of the diverging behavior of the Au (Au, Pt, Pd) and Ru (Ru, Rh, Ir) groups regarding their preferred formation of metallic or oxidic nanoparticles relates to their ability to form stable oxides. To assess the impact of the metal-host interactions in the M/C catalysts, DFT was employed. The model for the AC and NC supports was constructed from 16 distinct defects containing either N (pyrrolic, pyridinic, graphitic, oxo-pyridinic) or O (hydroxyl, epoxide, keto) heteroatoms (**Supplementary Fig. 10,** see Computational Methods for details) leading to 280 metal-carbon configurations. This thorough speciation analysis is based on stability of the single atoms, chlorinated single atoms, bulk metals and metal oxides (that identify thermodynamically stable configurations, **Supplementary Fig. 11-15**) coupled to matching the experimental characterization fingerprints, EXAFS (narrowing further the set of most likely models, **Supplementary Fig. 16**). Considering this extensive number of sites offering diverse coordination motifs,

the interactions of a single-metal atom (MCl species) vary widely depending on the specific AC or NC defect (**Fig. 2b, Supplementary Fig. 17**). Remarkably, also the extent of this interaction, as averaged (arithmetic mean) formation energies of the non-chlorinated single atom M-SA (**Fig. 2b**) and chlorinated MCl (**Fig. 2c**) species, correlates with the metal oxide phase. Overall, this observation indicates a (linear) dependence between the metal, metal oxide, and metal SA (MCl) stability. Thereby, the metal oxide formation energy plays the key role in directing the speciation behavior. For example, on a representative bi-epoxidic AC defect, the stability of the SA species (with reference to the metal bulk) is sufficient to overcome the cohesive energy of all metals, if Cl is present in the coordination sphere (T_{act} = 473 K). Upon increasing the activation temperature, the Cl content decreases, leading to the formation of less stable Cl-undercoordinated SA species. For Ru in the two epoxidic defects described above this leads to MO_2 species attached to the surface *via* van der Waals (vdW) forces. These are then mobile and agglomerate into larger metal oxide particles. The stability of the Au group is also compromised by Cl removal. However, in contrast to the Ru group, the formation of MO_2 species is not favorable, thus leaving the epoxidic defect intact and promoting sintering of the Au group (**Fig. 2d**).

(II) Catalyst Preparation

The N-doped carbon support (NC) was prepared in a two-step synthesis, consisting of the oxidative polymerization of aniline and a subsequent carbonization step.[1] Aniline (50 mmol, Acros, 99.5%) was dissolved in deionized water (40 cm^3, pH 0.4; adjusted by hydrochloric acid, 1.25 M, Sigma Aldrich, >37%), cooled to 277 K, and subsequently added to a precooled solution (277 K) of ammonium persulfate (50 mmol, Acros, 98%) in deionized water (20 cm^3). After 5 min of vigorous stirring, the mixture was kept at room temperature for 24 h to complete the polymerization process. The formed polyaniline was thoroughly washed with deionized water for neutralization, dried in vacuum at 393 K for 12 h, and afterwards calcined at 1073 K (heating rate 5 K min^{-1}, hold time 1 h, static N_2). The obtained N-doped carbon was ground and sieved (particle size 0.4-0.6 mm). Commercial activated carbon (AC, Norit ROX 0.8) was immersed in aqua regia at room temperature to remove metal impurities. After filtration and

thorough washing with deionized water (750 $cm^3\ g^{-1}$), the material was dried in static air at 393 K for 12 h and subsequently ground and sieved into 0.4-0.6 mm particles.

All metal-based catalysts were prepared *via* an incipient wetness impregnation method with a nominal metal loading of 1 wt.%. The metal precursors, $HAuCl_4{\cdot}xH_2O$ (ABCR, 99.9%, 49.5 wt.% Au), $RuCl_3{\cdot}xH_2O$ (ABCR, 99.9%, 40.0 wt.% Ru), H_2PtCl_6 (ABCR, 99.9%, 40.0 wt.% Pt), $IrCl_3{\cdot}xH_2O$ (ABCR, 99.9%, 65 wt.% Ir), $RhCl_3{\cdot}xH_2O$ (ACROS Organics, 99.9%, 38 wt.% Rh), and $PdCl_2$ (Sigma Aldrich, 99.9%, 60 wt.% Pd) were dissolved in aqua regia (1.5 $cm^3\ g^{-1}$ Au, 5-8 $cm^3\ g^{-1}$ for Ru, Ir, Rh), HCl (1.5 $cm^3\ g^{-1}$ for Pd) or water (1.5 $cm^3\ g^{-1}$ for Pt) and the obtained solutions were added dropwise, under magnetic stirring, to the carbon carriers. Subsequently, all samples were dried at 473 K (heating rate = 5 K min^{-1}, hold time 12 h, static air) to yield the respective single-atom catalysts, denoted as M-SA/NC or M-SA/AC. In the case of Au, Pt, and Pd, single atoms with four-fold N-coordination (M-SA-N_4/NC) were obtained *via* thermal activation of the respective M-SA/NC samples (T_{act} = 1073 K, heating rate = 5 K min^{-1}, 16 h, flowing N_2). Nanoparticle-based M/C catalysts with varying particle sizes were derived *via* thermal activation in the temperature range of T_{act} = 523-1073 K (heating rate = 5 K min^{-1}, hold time 12 h, flowing N_2). For each metal, a representative nanoparticle-based sample (M-NP/NC for Ru, Rh, Ir or M-NP/AC for all metals) was selected (*i.e.*, the system with the highest activity for Ru-, Ir-, Rh-, and Pd-based catalysts and a sample of comparable particle size for Au and Pt-based catalysts). Catalysts after use in acetylene hydrochlorination for *x*-h time-on-stream (*tos*) are labeled M/C-*x*h.

(III) Catalyst Characterization

Powder X-ray diffraction (XRD) was measured using a PANalytical X'Pert PRO-MPD diffractometer with Cu-Kα radiation (λ = 1.54060 Å). The data was recorded in the 10-70° 2θ range with an angular step size of 0.017° and a counting time of 0.26 s per step. Ar sorption isotherms were measured at 77 K in a Micromeritics 3Flex instrument, after degassing of the solids at 423 K for 12 h. Scanning transmission electron micrographs (STEM) with a high-angle annular dark-field (HAADF) detector were acquired on an aberration-corrected HD2700CS (Hitachi) microscope operated at 200 kV. Samples were prepared by

dipping the copper grid supporting a holey carbon foil in a suspension of the solid in ethanol and drying in air. X-ray photoelectron spectra (XPS) were acquired on a Physical Electronics Quantum 2000 instrument using monochromatic Al-Kα radiation, generated from an electron beam operated at 15 kV, and equipped with a hemispherical capacitor electron-energy analyzer. The samples were analyzed at an electron take-off angle of 45° and a constant analyzer pass energy of 46.95 eV with a spectra resolution step width of 0.2 eV. The spectrometer was calibrated for the Au $4f_{7/2}$ signal at 84.0 ± 0.1 eV. The Au 4*f*, Pt 4*f*, Pd 3*d*, Ru 3*p*, Rh 3*d*, and Ir 4*f* spectra were fitted by mixed Gaussian-Lorentzian component profiles after Shirley background subtraction. The selected peak positions are based on literature reported data. X-ray absorption fine structure (XAFS) measurements were carried out at the SuperXAS beamline of the Swiss Light Source.[2] The incident photon beam provided by a 2.9 T superbend magnet was selected by a Si(111) channel-cut Quick-EXAFS monochromator.[3] The rejection of higher harmonics and focusing were achieved with Rh-coated (for Ir-L_3, Pt-L_3, Au-L_3 edges) and a Pt-coating (for Pd-*K*, Ru-*K*, and Rh-*K* edges), respectively, at 2.5 mrad. The beamline was calibrated using the respective metal foils. The area of sample illuminated by the X-ray beam was 0.5 mm×0.2 mm. All spectra were recorded in transmission mode at room temperature. The extended X-ray absorption fine structure (EXAFS) spectra were acquired with a 1 Hz frequency (0.5 s per spectrum) and then averaged over 10 min. The resulting raw data were processed using the ProQEXAFS software package.[4] The EXAFS spectra were analyzed using the Demeter software package.[5] Volumetric chemisorption of acetylene at 473 K (W_{cat} = 0.1 g) was performed in a Micromeritics 3Flex Chemi instrument to quantify the amount of acetylene chemisorbed (V_{chem}) at reaction temperature. Thermogravimetric analysis (TGA) was performed using a Linseis STA PT1600 system coupled to a Pfeiffer Vacuum Thermo-Star GSD 320 T1 mass spectrometer. TGA of the as-prepared catalysts and after use in acetylene hydrochlorination was carried out in diluted oxygen (20 vol.% O_2/Ar, 100 cm^3 min^{-1}), heating the samples (amount fixed to 20 mg) from 298 to 1273 K at 10 K min^{-1} to quantify the amount of coke in the used catalysts.

(IV) Catalytic Evaluation

The hydrochlorination of acetylene was evaluated at atmospheric pressure in a continuous-flow fixed-bed micro-reactor (**Supplementary Fig. 28**). The gases C_2H_2 (PanGas, purity 2.6), HCl (Air Liquide, purity 2.8, anhydrous), Ar (PanGas, purity 5.0, internal standard), and He (PanGas, purity 5.0, carrier gas), were fed using digital mass-flow controllers (Bronkhorst) to the mixing unit, equipped with a pressure indicator. A quartz micro-reactor of 10 mm inner diameter was loaded with the catalyst (W_{cat} = 0.1 g in initial catalytic activity tests and kinetic tests, and 0.25 g in stability tests, particle size 0.4-0.6 mm) and placed in a homemade electrical oven. A K-type thermocouple fixed in a coaxial quartz thermowell with the tip positioned in the center of the catalyst bed was used to control the temperature during the reaction. Prior to testing, the catalyst was heated in a He flow to the desired bed temperature (T_{bed} = 473 K) and allowed to stabilize for at least 30 min before the reaction mixture (40 vol.% C_2H_2, 44 vol.% HCl, and 16 vol.% Ar) was fed at a total volumetric flow of F_T = 15 cm^3 min^{-1}. Reaction kinetics of acetylene hydrochlorination over selected M/C catalysts were studied at conversion levels <20% in the temperature range of 453-483 K with a total flow of F_T = 20 cm^3 min^{-1} and reactant concentrations of 10-30 vol.% balanced in He to determine the apparent activation energy (E_a) and the partial reaction order of the reactants ($n_{C_2H_2}$, n_{HCl}). Carbon-containing compounds (C_2H_2 and C_2H_3Cl) and Ar were quantified on-line *via* a gas chromatograph equipped with a GS-Carbon PLOT column coupled to a mass spectrometer (GC-MS, Agilent, GC 7890B, Agilent MSD 5977A). Since vinyl chloride (VCM) was the only product detected in all our tests, the catalytic activity is presented as the yield of VCM, *Y*(VCM), calculated according to Eq. 1,

$$Y(\mathrm{VCM}),\% = \frac{n_{\mathrm{VCM}}^{\mathrm{outlet}}}{n_{\mathrm{C_2H_2}}^{\mathrm{inlet}}} \cdot 100 \qquad \text{Eq. 1}$$

where $n_{\mathrm{VCM}}^{\mathrm{outlet}}$ and $n_{\mathrm{C_2H_2}}^{\mathrm{inlet}}$ denote the molar flows of VCM and C_2H_2 at the reactor outlet and inlet, respectively. The VCM yield determined after 15 min *tos* (during initial activity tests) is denoted as Y^0(VCM). The reaction rate (*r*) and turnover frequency (*TOF*) were determined according to Eq. 2 and 3,

$$r, \mathrm{mol}_{C_2H_2}\ \mathrm{s}^{-1}\ \mathrm{g}_{cat}^{\ -1} = \frac{n_{C_2H_2}^{inlet} - n_{C_2H_2}^{outlet}}{W_{cat}} \quad \text{Eq. 2}$$

$$TOF, \mathrm{mol}_{C_2H_2}\ \mathrm{s}^{-1}\ \mathrm{mol}_{site}^{\ -1} = \frac{n_{C_2H_2}^{inlet} - n_{C_2H_2}^{outlet}}{n_M \cdot D_M} \quad \text{Eq. 3}$$

where W_{cat} denotes the catalyst mass and n_M the amount of metal in moles. D_M indicates the metal dispersion, which was set to 100% for single-atom catalysts and estimated from the average metal particle size for nanoparticle-based catalysts. The error of the carbon balance, ε_C, determined using Eq. 4, was less than 5% in all experiments, *i.e.*, the carbon mass balance was closed at ≥ 95%.

$$\varepsilon_C, \% = \frac{n_{C_2H_2}^{inlet} - \left(n_{C_2H_2}^{outlet} + n_{VCM}^{outlet}\right)}{n_{C_2H_2}^{inlet}} \cdot 100 \quad \text{Eq. 4}$$

After the tests, the reactor was quenched to room temperature in He flow and the catalyst was retrieved for further characterization. All catalytic data points were determined as an average of at least three measurements. Each catalytic test presented in this study was performed in the absence of mass and heat transfer limitations, as confirmed by experimental and theoretical evaluation based on the criteria of Carberry,[6] Mears,[7] and Weisz-Prater.[8] (see for details the following section and **Supplementary Table 11**). The deactivation constants, k_D, were derived *via* a simple linear regression of the data range within the first 1 and 10 h time-on-stream in acetylene hydrochlorination ($k_{D,1h}$ and $k_{D,10h}$, **Supplementary Table 1**).

(V) Assessment of Mass and Heat Transfer Limitations

The Carberry criterion (*Ca*)[6] was used to evaluate external mass transfer limitations according to Eq. 5,

$$Ca = \frac{r_{v,obs}}{a' \cdot k_f \cdot c_b} < \frac{0.05}{|n|} \quad \text{Eq. 5}$$

where k_f is the mass transfer coefficient (estimated at a minimum value of 0.01 $\mathrm{m\ s^{-1}}$), c_b is the bulk concentration of acetylene (17.6 $\mathrm{mol}_{C_2H_2}\ \mathrm{m^{-3}}$), *n* the reaction order, and $r_{v,obs}$ and a' denote the reaction rate and the specific particle area, which are derived *via* Eq 6 and Eq. 7, respectively,

$$r_{\mathrm{v,obs}} = \frac{n_{\mathrm{C_2H_2}}^{\mathrm{inlet}} - n_{\mathrm{C_2H_2}}^{\mathrm{outlet}}}{V_{\mathrm{cat}}} \qquad \text{Eq. 6}$$

$$a' = \frac{1}{L} = \frac{A_{\mathrm{p}}}{V_{\mathrm{p}}} = \frac{6}{d_{\mathrm{p}}} \qquad \text{Eq. 7}$$

To assess external temperature differences (ΔT_{e})[6] Eq. 8 was applied,

$$\Delta T_{\mathrm{e}} = \beta_{\mathrm{e}} \cdot Ca = \frac{\left(-\Delta H_{\mathrm{r}}\right) \cdot k_{\mathrm{f}} \cdot c_{\mathrm{b}}}{h \cdot T_{\mathrm{b}}} Ca \qquad \text{Eq. 8}$$

where β_{e} denotes the external Prater number, T_{b} the temperature in the bulk material (473 K), h the heat transfer coefficient (estimated at a minimum value of 10 J m^{-2} s^{-1} K^{-1}), and ΔH_{r} the reaction enthalpy (99.3 kJ mol^{-1}). Internal mass transfer limitations were evaluated using the Weisz-Prater criterion (Φ),[8] according to Eq. 9,

$$\Phi = \frac{r_{\mathrm{v,obs}} \cdot L^2}{D_{\mathrm{eff}} \cdot c_{\mathrm{s}}} \left(\frac{n+1}{2} \right) < 1 \qquad \text{Eq. 9}$$

Where L is the characteristic length (0.25 mm), c_{s} the surface concentration ($c_{\mathrm{s}} \approx c_{\mathrm{b}}$ in the absence of external mass transfer limitations), and D_{eff} the effective diffusion coefficient, which can be derived *via* Eq. 10,

$$D_{\mathrm{eff}} = \frac{\varepsilon}{\tau} \cdot \overline{D} = \left(\frac{1}{D_{\mathrm{C_2H_2,HCl}}} + \frac{1}{D_{\mathrm{K}}} \right)^{-1} \qquad \text{Eq. 10}$$

where τ is the tortuosity factor (estimated at 3), ε is the particle porosity (estimated at 0.2), $D_{\mathrm{C_2H_2,HCl}}$ is the molecular diffusion coefficient (1.96 10^{-5} m^2 s^{-1}), and D_{K} is the Knudsen diffusion coefficient which is calculated for components i (i = HCl, C_2H_2) in a cylindrical pore according to Eq. 11,

$$D_{\mathrm{K},i} = 97 \cdot r_{\mathrm{pore}} \cdot \sqrt{\frac{T}{M_i}} \qquad \text{Eq. 11}$$

where r_{pore} denotes the pore radius, M_{i} the molecular weight of component i, and T the temperature (473 K). Intra-particle temperature differences (ΔT_{i}) can be calculated using Eq. 12,[7]

$$\Delta T_i = \beta_i \cdot T_s = \frac{\left(-\Delta H_r\right) \cdot D_{eff} \cdot c_s}{\lambda_{eff}} \qquad \text{Eq. 12}$$

where β_i denotes the internal Prater number and λ_{eff} the effective thermal conductivity (estimated at 0.5 W K^{-1} min^{-1}). The results for Pt/C catalysts are given in **Supplementary Table 11**. For all catalytic tests, the Carberry criterion (Eq. 5) is fulfilled and hence no external mass transfer limitations are present. In line with this result, the external temperature difference is negligible (< 0.01 K), indicating the absence of external heat transfer limitations. In the fresh M/C catalysts, intra-particle mass transfer limitations are largely negligible, while with decreasing pore size minor diffusional disguises might develop for M/NC catalysts, which are partially compensated by the simultaneous drop in the reaction rate. Only for pore sizes < 0.1 nm internal mass transfer limitations become dominant. Finally, the temperature gradient within the catalyst particle is negligible for each case, indicating the absence of internal heat transfer limitations.

(VI) Transient Mechanistic and Kinetic Analyses

The interactions of C_2H_2, HCl, and VCM with the bare supports (NC and AC) and selected gold, platinum, ruthenium, iridium, rhodium, and palladium-based catalysts were studied in the Temporal Analysis of Products (TAP-2) reactor system. This transient pulse technique operates in high vacuum with a time resolution of approximately 100 μs.[9-11] Each catalyst (W_{cat} = 13 mg, particle size 0.4-0.6 mm) was packed between two layers of quartz particles (size 0.25-0.35 mm) within the isothermal zone of an in-house (Leibniz-Institut für Katalyse) developed fixed-bed quartz micro-reactor. Afterwards, the reactor was evacuated to 10^{-5} Pa. The pulse experiments were carried out at 473 K using C_2H_2:Ne = 1:1, HCl:Ar = 1:1, and C_2H_3Cl:Ar = 1:1 mixtures prepared from C_2H_2 (Air Liquide, 2.6), HCl (Air Liquide, 4.5), VCM (Sigma Aldrich International GmbH, 99.95%), Ne (Linde Gas, 5.0), and Ar (Linde Gas, 5.0) without additional purification. The feed components were quantified by an on-line quadrupole mass spectrometer (HAL RC 301 Hiden Analytical). The following atomic mass units (AMUs) were assigned for mass spectrometric identification: 70 (Cl_2), 64 (C_2H_3Cl), 62 (C_2H_3Cl), 36 (HCl), 28 (CO), 27 (C_2H_3Cl, C_2H_2), 26 (C_2H_3Cl, C_2H_2), 22 (Ne), 2 (H_2), 40 (Ar), and 20 (Ar, Ne). The overall pulse size was below

2×10^{15} molecules. Pulses were repeated ten times for each AMU and averaged to improve the signal-to-noise ratio.

To identify the type of adsorption (reversible or irreversible), the obtained transient responses of reactive and inert gases were transformed into a dimensionless form as suggested in reference [9]. The comparison of the relative position of the transformed signals of the inert gas and reactive component allows distinguishing between different types of adsorption. If the transformed signal of the reactive component is situated under and does not cross that of the transformed inert gas, the former adsorbs irreversibly or is consumed. Intersection of the curves indicates reversible adsorption (**Supplementary Scheme 1**). The obtained responses are summarized in **Supplementary Figs. 19-22**. Kinetic evaluation of the TAP experiments, *i.e.* fitting experimental data to chosen kinetic models, was performed as detailed elsewhere.[10] According to this approach, the TAP micro-reactor is described as a one-dimensional pseudo-homogeneous system. The search for kinetic parameters (*i.e.*, the effective adsorption, $k_{ads,eff}$, and desorption constants, k_{des}, and their ratio K) was performed in a wide range of possible values (10^{-4}-10^{6}) using first a Genetic algorithm[12] and subsequently the Nelder-Mead Simplex algorithm.[13] The estimated parameters were validated by applying correlation and sensitivity analyses. The correlation analysis shows if the parameters do not influence each other, otherwise only their product or ratio can be determined definitively. In the present study, the overall concentration of active sites and the rate constant of adsorption are depending on each other. Thus, only their product, denoted as $k_{ads,eff}$, could be determined. The sensitivity analysis defines the effect of changes of the corresponding parameter on the objective function. When the change of the parameter has no influence on the objective function, the respective reaction step should be refused to avoid over-parameterization of the model.

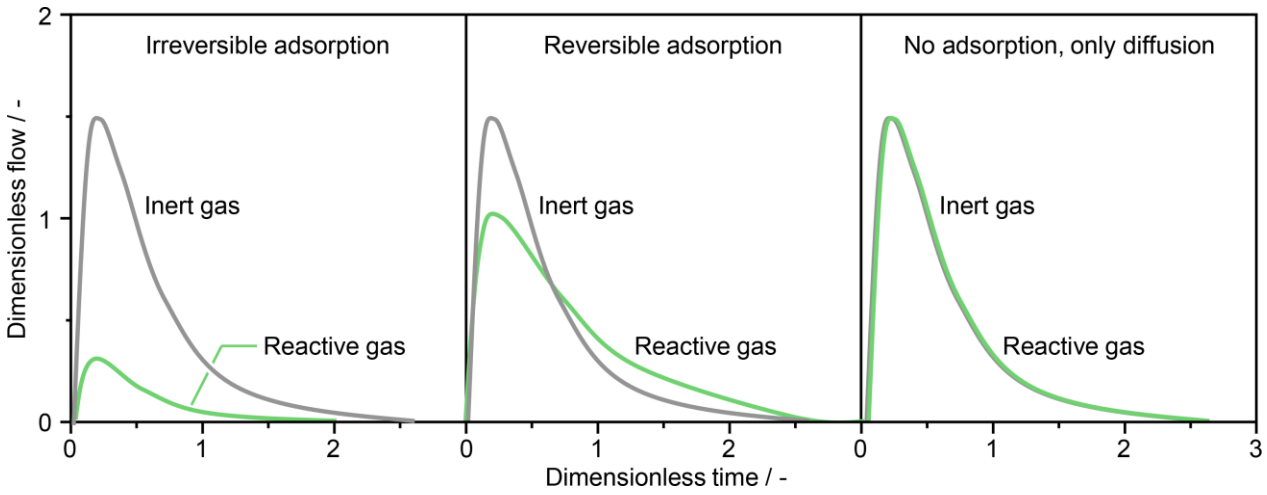

Supplementary Scheme 1. Possible adsorption modes of reactive gases as determined by analysis of transient responses transformed according to ref. 9.

(VII) Computational Methods

Density functional theory (DFT) simulations were performed utilizing the Vienna *Ab initio* simulation package (VASP) code.[14] The functional of choice was Perdew-Becke-Ernzerhof (PBE).[15] Dispersion contributions were introduced through the D3 approach.[16] Inner electrons were described by projector augmented-waves (PAW)[17] and the valence monoelectronic states expanded as plane waves with a cutoff kinetic energy of 450 eV. Graphite slabs were modeled using a (6×6) supercell comprising three layers, interleaved by 12 Å of vacuum, relaxation was allowed only for the top two layers. The *k*-points sampling was a Γ–centered 3×3×1 grid. The models for the cavities were constructed from 16 distinct defects containing either N (pyrrolic, pyridinic, graphitic, oxo-pyridinic) or O (hydroxyl, epoxide, keto) heteroatoms as shown in **Extended Data Fig. 1**. These sites were populated by 6 different metals as single atoms, chlorinated single atoms, and metal dimers and evaluated based on stability (*i.e.*, formation energies, dimer formation energies, chlorine affinity) and activity (*i.e.*, steric prerequisites, availability of free coordination sites at the single-atom center) descriptors (**Supplementary Figs. 10-14)**. Following this exhaustive analysis, we retained only the two most representative sites, bi-epoxidic for AC and tri-pyrrolic for NC. We assessed the uncertainties in acetylene adsorption energies at the epoxidic and pyrrolic SA sites by substituting one of the defect heteroatoms (O, N) with C (**Supplementary Fig. 29**). To test the

validity of our models, we have computed the simulated EXAFS spectra for the selected structural motifs (**Supplementary Fig. 15**), allowing us to make a direct comparison between experiments and theory. While fine features found in the simulated spectra are not present in the measurements due to averaging effects (over metal centers with different anchors/coordination spheres), the main features are well aligned (generally the main peak at ~2 Å with a shoulder at ~1.5 Å). Selecting representative and uniform defects for AC and NC-based catalysts enabled us to minimize errors arising from the single-atom site reconfiguration upon adsorption (as different sites for AC and NC result in variable degrees of local relaxation when perturbed by an interacting adsorbate). Due to this, we put forward that the selection of our models is likely to enhance the overall reliability of the C_2H_2 adsorption calculations. All structures can be retrieved from the ioChem-BD database.[18] Link for Reviewers: https://iochem-bd.iciq.es/browse/review-collection/100/29192/2e648deedac4405e0196efac.

Supplementary Table 1. Synthesis details of the M/C catalysts, initial yield of vinyl chloride monomer (Y^0(VCM)), and deactivation constants (k_D) in acetylene hydrochlorination.

Catalyst[a]	Solvent	T_{act}[b] / K	Y^0(VCM)[c] / %	$k_{D,1h}$[d] / h^{-1}	$k_{D,3h}$[e] / h^{-1}	$k_{D,10h}$[f] / h^{-1}
Au-SA/AC	aqua regia	473	59	-0.6	-0.3	-1.6
Au-NP/AC	aqua regia	623	8	0	0	-
Au-SA/NC	aqua regia	473	60	-1.2	-0.5	-
Au-SA-N_4/NC	aqua regia	1073	35	-0.5	-	-
Pt-SA/AC	water	473	26	-1.5	-0.1	-0.2
Pt-NP/AC	water	1073	6	-0.3	-0.1	-
Pt-SA/NC	water	473	29	-2.1	-0.5	-3.2
Pt-SA-N_4/NC	water	1073	15	-0.5	-	-
Pd-SA/AC	HCl	473	1	-34.8	-4.1	-
Pd-NP/AC	HCl	673	3	-43.8	-0.4	-0.2
Pd-SA/NC	aqua regia	473	5	-59.4	-8.4	-
Pd-SA-N_4/NC	aqua regia	1073	13	-35.8	-	-
Ru-SA/AC	aqua regia	473	13	-13.8	-5.2	-
Ru-NP/AC	aqua regia	1073	26	-14.4	-5.7	-3.1
Ru-SA/NC	aqua regia	473	29	-13.2	-6.3	-
Ru-NP/NC	aqua regia	1073	56	-21.6	-17.7	-6.7
Rh-SA/AC	aqua regia	473	14	-28.8	-6.6	-
Rh-NP/AC	aqua regia	873	29	-30.6	-6.4	-2.4
Rh-SA/NC	aqua regia	473	11	-16.2	-4.0	-
Rh-NP/NC	aqua regia	873	25	-13.2	-5.3	-2.1
Ir-SA/AC	aqua regia	473	13	-22.8	-6.2	-
Ir-NP/AC	aqua regia	873	17	-16.2	-5.9	-1.9
Ir-SA/NC	aqua regia	473	11	-10.2	-6.0	-
Ir-NP/NC	aqua regia	1073	32	-18.0	-4.8	-2.0

[a]SA: single atoms; SA-N_4: single atoms with 4-fold N-coordination; NP: nanoparticles; AC: activated carbon; NC: N-doped carbon. [b]Temperature applied during thermal activation of the impregnated metal catalyst. [c]Initial activity at $GHSV(C_2H_2)$ = 1500 h^{-1}. [d-f]Deactivation constants derived *via* linear regression in the data range of the initial 1, 3, and 10 h on stream at $GHSV(C_2H_2)$ = 650 h^{-1}.

Supplementary Table 2. Au 4*f*, Pt 4*f*, Pd 3*d*, Ru 3*p*, Rh 3*d*, and Ir 4*f* XPS fitting parameters.

Component	Position[a] / eV	FWHM[b] / eV	Reference
Au(0)	82.4	1.1 ± 0.1	19
Au(I)	85.0	1.4 ± 0.1	19
Pt(0)	71.2	1.1 ± 0.1	20
Pt(II)	72.4	2.0 ± 0.1	20
Pt(IV)	73.6	2.3 ± 0.2	20
Pd(0)	335.1	1.0 ± 0.1	21,22
Pd(II)	337.3	2.2 ± 0.1	21,22
Ru(0)	461.2	2.0 ± 0.1	23
Ru(III)-Cl	464.3	2.9 ± 0.2	23
Ru(IV)-O	462.8	2.0 ± 0.2	23
Rh(0)	307.2	1.2 ± 0.1	24-27
Rh(III)-O	308.4	1.4 ± 0.1	24-27
Rh(III)-Cl	309.8	2.1 ± 0.1	24-27
Ir(0)	60.8	1.4 ± 0.1	28
Ir(III)	62.1	1.7 ± 0.2	28

[a]Assigned based on reference values. [b]FWHM: full width at half maximum.

Supplementary Table 3. Elemental surface concentrations determined by XPS of the fresh and used M/C catalysts.

Catalyst	C / at.%	N / at.%	O / at.%	Cl /at.%
Au-SA/AC	91.0	0.5	7.8	0.7
Au-SA/AC-12h	91.9	0.6	6.6	0.9
Au-SA/NC	79.5	10.4	8.6	1.5
Au-SA/NC-12h	81.5	9.1	8.1	1.3
Pt-SA/AC	95.0	0.4	4.2	0.2
Pt-SA/AC-12h	96.0	0.4	2.7	0.8
Pt-SA/NC	85.8	8.5	5.1	0.6
Pt-SA/NC-12h	86.4	8.0	4.3	1.3
Pd-NP/AC	96.1	0.2	3.6	0.2
Pd-NP/AC-12h	95.9	0.2	3.5	0.6
Ru-NP/AC	93.4	0.4	4.6	0.2
Ru-NP/AC-12h	92.5	0.5	5.0	1.1
Ru-NP/NC	87.4	7.7	4.5	0.1
Ru-NP/NC-12h	88.4	7.0	2.4	1.9
Rh-NP/AC	96.1	0.1	3.1	0.6
Rh-NP/AC-12h	95.5	0.1	3.2	1.3
Rh-NP/NC	83.1	9.9	4.7	0.4
Rh-NP/NC-12h	85.2	8.5	2.9	1.3
Ir-NP/AC	96.6	0.2	3.1	0.0
Ir-NP/AC-12h	97.4	0.1	2.0	0.5
Ir-NP/NC	86.8	8.3	3.0	0.1
Ir-NP/NC-12h	85.4	7.6	2.9	2.0

Supplementary Table 4. Fitting parameters derived from EXAFS data of M/AC catalysts.

Catalyst	Coordination shell	CN[a] / -	σ^{2b} / Å^2	R^c / Å
Au-SA/AC	Au-Cl	2.5 ± 0.2	0.003 ± 0.002	2.27 ± 0.03
Au-NP/AC	Au-Cl	0.4 ± 0.1	0.0036[d]	2.23 ± 0.05
	Au-Au	9.3 ± 0.9	0.003 ± 0.002	2.85 ± 0.02
Pt-SA/AC	Pt-Cl	3.2 ± 0.3	0.005 ± 0.002	2.29 ± 0.01
	Pt-O/C	0.5 ± 0.2	0.006 ± 0.002	1.98 ± 0.03
Pt-SA/AC-12h	Pt-Cl	3.1 ± 0.3	0.005 ± 0.002	2.29 ± 0.01
	Pt-O/C	0.3 ± 0.1	0.006 ± 0.002	1.96 ± 0.03
Pd-SA/AC	Pd-Cl	3.8 ± 0.4	0.004 ± 0.002	2.31 ± 0.03
Pd-NP/AC	Pd-Pd	8.1 ± 0.8	0.006 ± 0.003	2.74 ± 0.03
Ru-SA/AC	Ru-O/C	2.5 ± 2.3	0.002 ± 0.004	2.03 ± 0.02
	Ru-Cl	3.2 ± 2.4	0.005 ± 0.004	2.35 ± 0.02
Rh-SA/AC	Rh-Cl	3.7 ± 0.5	0.003[e]	2.30 ± 0.03
	Rh-O/C	3.0 ± 0.5	0.002[e]	2.05 ± 0.02
Rh-NP/AC	Rh-Cl	1.8 ± 0.5	0.003[e]	2.32 ± 0.03
	Rh-O/C	1.0 ± 0.4	0.002[e]	1.96 ± 0.03
	Rh-Rh	2.0 ± 0.2	0.006 ± 0.003	2.69 ± 0.02
Ir-SA/AC	Ir-Cl	5.4 ± 0.3	0.003 ± 0.001	2.31 ± 0.03
	Ir-O/C	0.4 ± 0.3	0.003 ± 0.001	2.08 ± 0.02
Ir-NP/AC	Ir-Ir	2.0 ± 0.5	0.010 ± 0.004	3.10 ± 0.03
	Ir-O/C	4.0 ± 0.3	0.009 ± 0.001	2.01 ± 0.02

[a]Coordination number. [b]Debye-Waller factor. [c]Coordination shell distance. [d]Fixed parameter derived from fitting of $HAuCl_4$ reference sample used to minimize the cross correlation between the coordination number and the Debye-Waller factor, due to the limited Au-Cl coordination. [e]Single scattering held at the refined value due to high correlating parameters.

Supplementary Table 5. Fitting parameters derived from EXAFS data of M/NC catalysts.

Catalyst	Coordination shell	CN[a] / -	σ^{2b} / Å^2	R^c / Å
Au-SA/NC	Au-Cl	2.0 ± 0.2	0.003 ± 0.002	2.27 ± 0.02
Au-SA-N_4/NC	Au-N/O/C	2.7 ± 0.6	0.006 ± 0.002	1.98 ± 0.02
Pt-SA/NC	Pt-Cl	2.3 ± 0.3	0.004 ± 0.002	2.29 ± 0.01
	Pt-N/O/C	1.2 ± 0.3	0.005 ± 0.002	1.97 ± 0.02
	Pt-Pt	0.2 ± 0.2	0.005 ± 0.002	2.93 ± 0.01
Pt-SA/NC-12h	Pt-Cl	3.0 ± 0.3	0.005 ± 0.002	2.29 ± 0.01
	Pt-N/O/C	0.4 ± 0.2	0.006 ± 0.002	1.95 ± 0.03
Pt-SA-N_4/NC	Pt-Cl	0.2 ± 0.1	0.005 ± 0.002	2.29 ± 0.01
	Pt-N/O/C	2.5 ± 0.1	0.006 ± 0.002	1.97 ± 0.03
	Pt-Pt	1.0 ± 0.5	0.005 ± 0.002	2.29 ± 0.01
Pd-SA/NC	Pd-Cl	2.2 ± 0.2	0.004[d]	2.31 ± 0.03
	Pd-N/O/C	1.1 ± 0.2	0.003 ± 0.002	2.00 ± 0.02
Pd-SA-N_4/NC	Pd-N/O/C	2.8 ± 0.3	0.008 ± 0.002	1.97 ± 0.02
Ru-SA/NC	Ru-N/O/C	1.2 ± 1.4	0.001 ± 0.005	2.03 ± 0.02
	Ru-Cl	4.3 ± 1.3	0.005 ± 0.002	2.37 ± 0.01
Ru-NP/NC	Ru-Ru	3.8 ± 0.3	0.0052 ± 0.0004	2.67 ± 0.01
	Ru-N/O/C	2.2 ± 0.4	0.0057 ± 0.002	2.00 ± 0.01
Ru-NP/NC-6h	Ru-Ru	1.8 ± 0.5	0.007 ± 0.001	2.68 ± 0.01
	Ru-Cl	2.9 ± 0.4	0.007 ± 0.001	2.39 ± 0.01
Rh-SA/NC	Rh-Cl	3.0 ± 0.5	0.003[d]	2.33 ± 0.03
	Rh-N/O/C	3.0 ± 0.5	0.002[d]	2.04 ± 0.02
	Rh-Rh	0.5 ± 0.3	0.006 ± 0.002	2.68 ± 0.03
Rh-NP/NC	Rh-N/O/C	2.1 ± 0.2	0.002[d]	1.96 ± 0.02
	Rh-Rh	1.9 ± 0.2	0.006 ± 0.002	2.69 ± 0.03
Ir-SA/NC	Ir-Cl	4.3 ± 0.3	0.003 ± 0.001	2.31 ± 0.03
	Ir-N/O/C	1.1 ± 0.3	0.003 ± 0.001	2.02 ± 0.02
	Ir-Ir	1.6 ± 0.2	0.004[d]	2.84 ± 0.03
Ir-NP/NC	Ir-N/O/C	4.0 ± 0.3	0.004 ± 0.002	2.00 ± 0.02
	Ir-Ir	3.8 ± 0.4	0.010 ± 0.004	3.11 ± 0.04

[a]Coordination number. [b]Debye-Waller factor. [c]Coordination shell distance. [d]Single scattering held at the refined value due to high correlating parameters.

Supplementary Table 6. Physical and chemical bulk descriptors of examined metals.

Metal	PE^{a}	ARE^{b}	IE^{c} / eV	$E_{coh}{}^{d}$ / eV	EA^{e} / eV	$T_M{}^{f}$ / K	$E_{ads}{}^{g}$ / eV	$T_{ox}{}^{h}$ / K
Au	2.54	1.42	9.23	3.81	2.31	1337	-0.36	423
Pt	2.28	1.44	8.96	5.84	2.13	2041	-1.76	723
Pd	2.20	1.35	8.34	3.89	0.56	1828	-1.29	1023
Ru	2.20	1.42	7.36	8.03	1.05	2607	-1.78	1473
Rh	2.28	1.45	7.46	5.75	1.14	2237	-1.90	1373
Ir	2.20	1.55	8.97	6.94	1.56	2739	-1.54	1343

[a]Pauling electronegativity. [b]Allred Rochow electronegativity. [c]First ionisation energy. [d]Cohesive energy. [e]Electron affinity. [f]Melting point of the metal. [g]Adsorption of an isolated metal atom on pristine graphite. [h]Oxide decomposition temperature for Au_2O_3, PtO_2, PdO, RuO_2, Rh_2O_3, and IrO_2.

Supplementary Table 7. Kinetic parameters of M/C catalysts in acetylene hydrochlorination.

Catalyst	E_a[a] / kJ mol^{-1}	$n_{C_2H_2}$[b]	n_{HCl}[b]
Au-SA/AC	30.4	1.02	0.76
Au-NP/AC	52.7	0.75	0.98
Au-SA/NC	28.0	1.05	0.72
Pt-SA/AC	21.6	1.06	0.89
Pt-NP/AC	43.8	0.55	0.54
Pt-SA/NC	18.0	1.12	0.75
Ru-NP/AC	12.4	0.73	0.61
Ru-SA/NC	8.1	0.36	0.93
Ru-NP/NC	10.6	0.88	0.65

[a]Apparent activation energy. [b]Partial reaction orders of the reactants.

Supplementary Table 8. Adsorption and desorption constants of HCl, C_2H_2, and VCM using Temporal Analysis of Products.

Catalyst	HCl			C_2H_2			VCM		
	$k_{ads,eff}$ / s^{-1}	k_{des} / s^{-1}	K^c / -	$k_{ads,eff}$ / s^{-1}	k_{des} / s^{-1}	K^c / -	$k_{ads,eff}$ / s^{-1}	k_{des} / s^{-1}	K^c / -
AC	-[a]	-[a]	-[a]	5.5×10^3	4.5×10^2	12.3	8.1×10^4	13	6.2×10^3
Au-SA/AC	3.0×10^3	1.0×10^{-6}	3.0×10^9	5.0×10^2	1.6×10^2	3.1	7.1×10^6	1.2×10^5	58
Au-NP/AC	5.0×10^2	4.0×10^2	1.3	4.1×10^2	1.2×10^2	3.4	6.7×10^6	7.7×10^4	87
Pt-SA/AC	3.9×10^3	3.7×10^{-1}	2.7×10^4	3.1×10^2	68	4.6	2.2×10^3	32	68
Pt-NP/AC	5.6×10^5	2.7×10^2	1.3×10^3	5.2×10^2	13	4.4	-[b]	-[b]	-[b]
Pd-SA/AC	5.5×10^3	4.9×10^{-1}	1.1×10^4	-[a]	-[a]	-[a]	1.4×10^3	22	64
Pd-NP/AC	7.2×10^3	6.2	1.1×10^3	8.7×10^2	2.4×10^2	3.6	1.3×10^3	21	63
Ru-SA/AC	3.1×10^3	4.2×10^{-1}	8.9×10^4	4.1×10^2	9.7×10^1	4.2	1.1×10^3	1.8×10^{-1}	61
Ru-NP/AC	8.6×10^3	6	1.4×10^3	4.3×10^4	1.5×10^4	2.8	-[d]	-[d]	67
Rh-SA/AC	1.6×10^6	67	2.4×10^4	-[b]	-[b]	-[b]	9.9×10^2	18	55
Rh-NP/AC	6.0×10^5	1.7×10^2	3.4×10^3	9.0×10^2	0.12	7.7×10^3	1.3×10^3	20	65
Ir-SA/AC	1.7×10^4	1.8×10^{-1}	8.9×10^4	4.3×10^4	1.5×10^3	1.2	1.5×10^3	23	63
Ir-NP/AC	1.4×10^4	9.7	1.4×10^3	6.8×10^2	0.62	1.1×10^3	6.4×10^3	89	72
NC	-[a]	-[a]	-[a]	1.2×10^3	1.4×10^2	8.6	1.2×10^3	14	90.6
Au-SA/NC	8.0×10^3	2.0×10^{-3}	4.0×10^6	9.3×10^2	1.3×10^2	7.2	1.2×10^3	17	70.9
Au-SA-N_4/NC	-[a]	-[a]	-[a]	4.7×10^2	87	5.4	1.2×10^3	14	84.6
Pt-SA/NC	1.6×10^3	2.0×10^2	7.7	6.6×10^4	1.2	5.7×10^4	1.1×10^4	16	6.9×10^2
Ru-SA/NC	3.4×10^4	2.4	1.4×10^4	7.5×10^6	1.0×10^6	7.6	1.3×10^3	23	58
Ru-NP/NC	6.5×10^4	1.7	3.8×10^4	2.6×10^5	73	3.5×10^3	6.4×10^3	3.7	1.7×10^3
Rh-SA/NC	3.5×10^4	1.3	2.7×10^4	4.3×10^2	1.4×10^2	3.1	1.7×10^3	29	60
Rh-NP/NC	-[a]	-[a]	-[a]	6.2×10^2	23	28	2.2×10^3	23	98
Ir-SA/NC	4.0×10^4	1.3	3.1×10^4	4.9×10^2	1.2×10^2	4	1.7×10^3	18	98
Ir-NP/NC	-[a]	-[a]	-[a]	8.8×10^2	1.1×10^2	7.6	7.7×10^3	12	6.5×10^2

[a]Irreversible adsorption. [b]Fitting not satisfactory. [c]$K = k_{ads,eff}/k_{des}$. [d]Due to strong variations in the absolute values (15 independent fittings), only the ratio K can be determined.

Supplementary Table 9. Porous properties of fresh and used M/C catalysts.

Catalyst	Fresh M/C catalyst			Used M/C catalyst, *tos* = 3 h		
	V_{total}[a] / $cm^3\ g^{-1}$	V_{micro}[b] / $cm^3\ g^{-1}$	S_{BET}[c] / $m^2\ g^{-1}$	V_{total}[a] / $cm^3\ g^{-1}$	V_{micro}[b] / $cm^3\ g^{-1}$	S_{BET}[c] / $m^2\ g^{-1}$
Au-SA/AC	0.60	0.54	1150	0.49	0.36	957
Au-NP/AC	0.65	0.51	1250	0.58	0.41	1002
Pt-SA/AC	0.66	0.57	1143	0.50	0.38	986
Pt-NP/AC	0.79	0.58	1280	0.62	0.44	1066
Pd-SA/AC	0.75	0.51	1187	0.02	0.00	11
Pd-NP/AC	0.72	0.55	1367	0.05	0.01	64
Ru-SA/AC	0.71	0.51	1276	0.29	0.18	488
Ru-NP/AC	0.75	0.56	1502	0.50	0.34	858
Rh-SA/AC	0.75	0.54	1473	0.37	0.24	630
Rh-NP/AC	0.71	0.59	1564	0.39	0.27	669
Ir-SA/AC	0.73	0.56	1371	0.29	0.17	485
Ir-NP/AC	0.76	0.62	1379	0.35	0.23	601
Au-SA/NC	0.27	0.15	398	0.32	0.16	327
Pt-SA/NC	0.22	0.13	385	0.33	0.14	308
Pd-SA/NC	0.21	0.14	334	0.02	0.00	6
Ru-SA/NC	0.22	0.15	376	0.16	0.005	50
Ru-NP/NC	0.24	0.16	399	0.21	0.06	179
Rh-SA/NC	0.23	0.17	370	0.18	0.02	75
Rh-NP/NC	0.27	0.20	382	0.22	0.08	211
Ir-SA/NC	0.23	0.17	357	0.32	0.12	319
Ir-NP/NC	0.20	0.12	327	0.27	0.07	188

[a]Volume of Ar adsorbed at $p/p_0 = 0.98$ and 77 K. [b]Micropore volume, *t*-plot method. [c]Total surface area, BET method.

Supplementary Table 10. Comparison of metal-based catalysts in acetylene hydrochlorination.

Catalyst	Metal / wt.%	V_{cat} / mL	W_{cat} / g	T_{bed} / K	$GHSV(C_2H_2)$ / h^{-1}	Y(VCM)[b] / %	$k_{D,1h}$[d] / h^{-1}	Reference
Au-SA/AC	1	0.5	0.25	473	650	90	-0.6	This work
Pt-SA/AC	1	0.5	0.25	473	650	45	-1.5	This work
Pd-NP/AC	1	0.5	0.25	473	650	10	-43.8	This work
Ru-NP/NC	1	0.5	0.25	473	650	89	-21.6	This work
Rh-NP/NC	1	0.5	0.25	473	650	40	-13.2	This work
Ir-NP/NC	1	0.5	0.25	473	650	42	-18	This work
Au/AC	1	n.a.[a]	0.2	453	870	24	-1	29
Pd/AC	1	n.a.[a]	0.2	453	870	12[c]	-7.5	29
Pt/AC	1	n.a.[a]	0.2	453	870	2	3	29
Ru/AC	1	n.a.[a]	0.2	453	870	15	-2.5	29
Rh/AC	1	n.a.[a]	0.2	453	870	5	-4	29
Ir/AC	1	n.a.[a]	0.2	453	870	15[c]	-7	29
Au/C-Acetone	1	n.a.[a]	0.09	473	17600	21	1	30
Au/NC	0.5	0.5	0.25	473	650	74	-1.3	19
Au-CeO_2/AC	1	n.a.[a]	n.a.[a]	453	720	98	n.a.[a]	31
Au-Sr/AC	1	1	n.a.[a]	453	762	88	-0.5	32
Pt/AC-w-473	1	n.a.[a]	0.25	473	650	60	-3	20
Ru@TPPB/AC	1	5	n.a.[a]	443	360	100	n.a.[a]	33
Ru-Co-Cu/SAC	0.1	5	n.a.[a]	443	180	99	n.a.[a]	34
Ru/NC-g	1	0.5	0.25	473	650	95	-5	23

[a]not available. [-b]Selectivity to vinyl chloride, S(VCM) >99% unless indicated otherwise. [c]S(VCM) = 96-97% due to coking. [d]Deactivation constants derived *via* linear regression in the data range of the initial 1 h on stream.

Supplementary Table 11. Results for mass and heat transfer limitation criteria for Au/C and Ru/C.

Catalyst	$r_{v,obs}$ [$mol_{C_2H_2}\ s^{-1}\ m_{cat}^{-3}$]	r_{pore}[a] [nm]	Ca[b] [-]	ΔT_e[c] [K]	Φ[d] [-]	ΔT_i[e] [K]
Au-SA/AC	7.1	2.2	0.003	0.009	0.92	0.14
Ru-NP/AC	3.4	2.3	0.002	0.006	0.41	0.15
Au-SA/NC	7.1	2.4	0.003	0.009	0.84	0.16
Ru-NP/NC	7.0	2.4	0.002	0.008	0.81	0.16

[a]Pore radius, estimated *via* nonlocal density functional theory. [b]Carberry criterion. [c]External temperature differences. [d]Weisz-Prater criterion. [e]Intra-particle temperature differences.

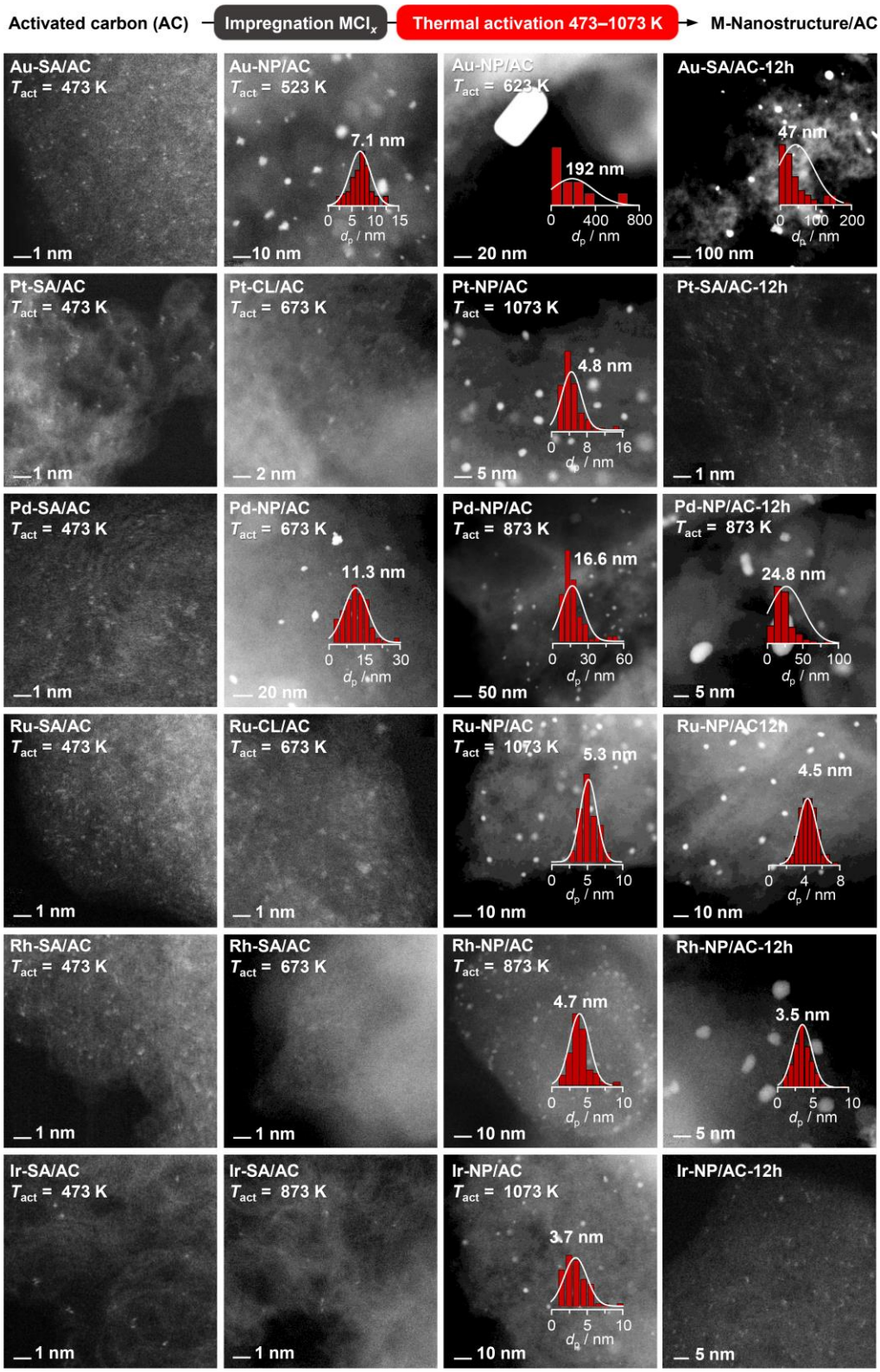

Supplementary Figure 1. STEM of fresh and used M/AC catalysts. Sample code: M: metal; SA: single atom; NP: nanoparticle; CL: cluster; T_{act}: activation temperature. Particle size distributions were derived from analysis of >100 particles.

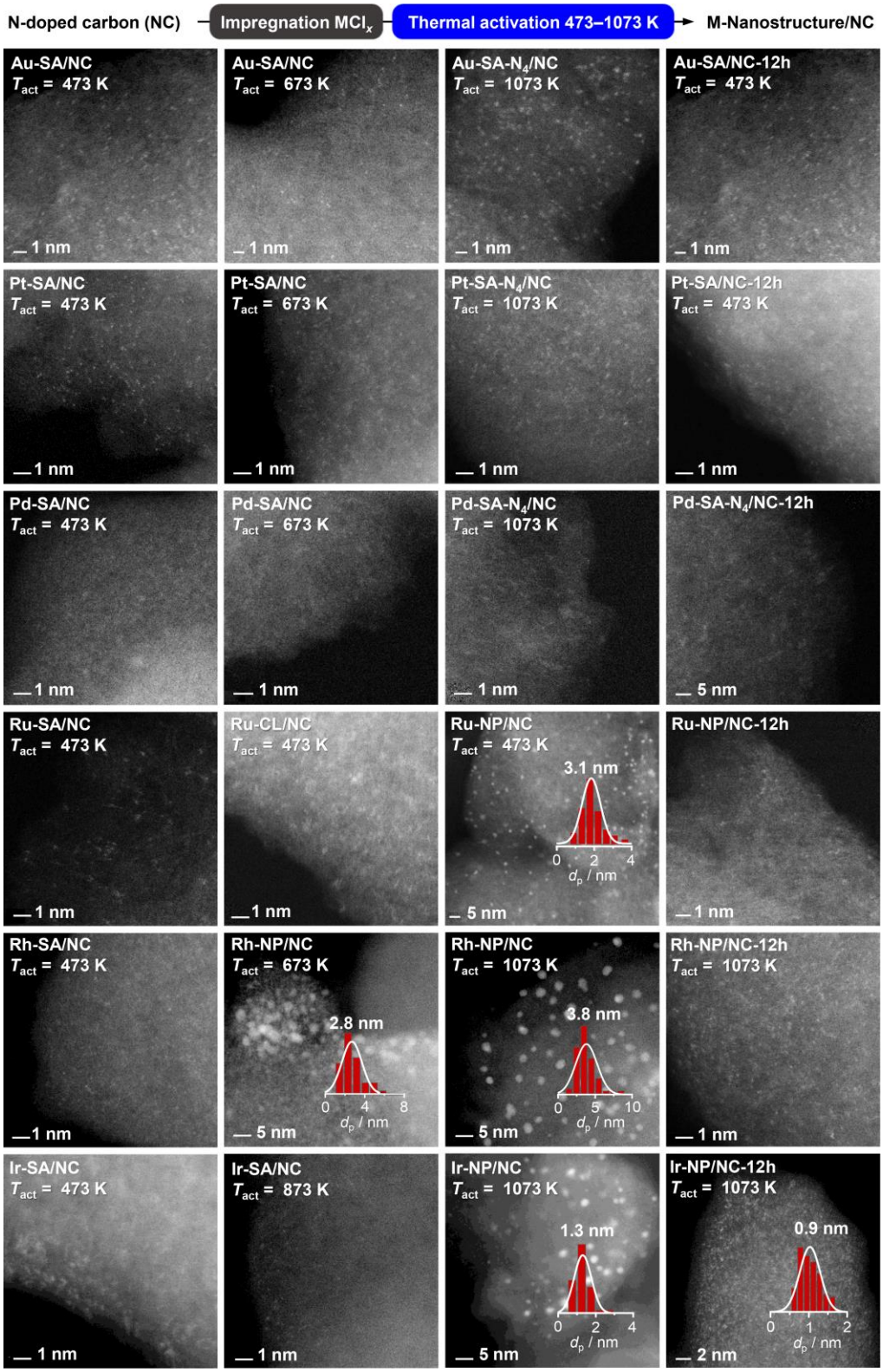

Supplementary Figure 2. STEM of fresh and used M/NC catalysts. Sample code: M: metal; SA: single atom; NP: nanoparticle; CL: cluster; T_{act}: activation temperature. Particle size CL: cluster. T_{act}: activation temperature. Particle size distributions were derived from analysis of >100 particles.

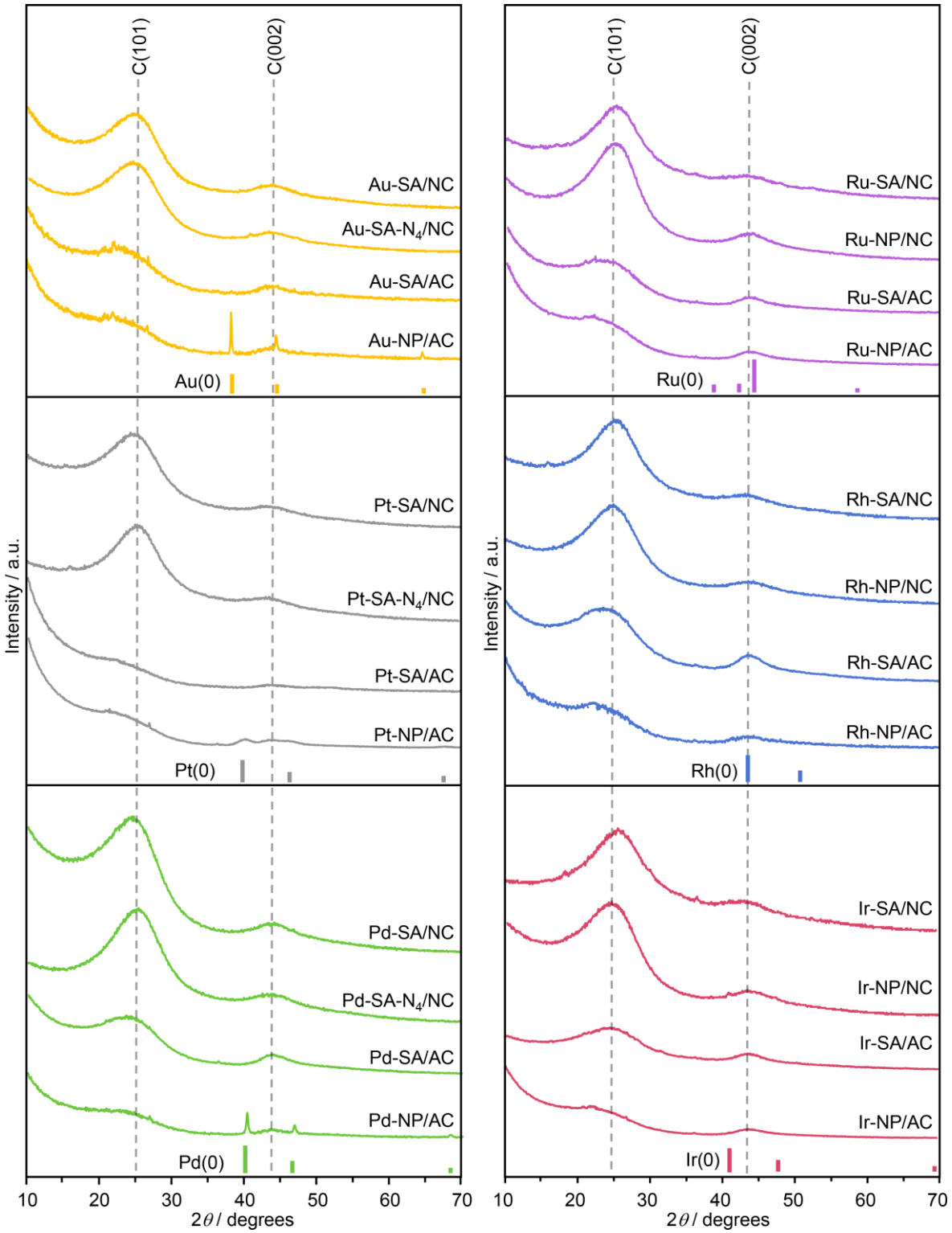

Supplementary Figure 3. XRD patterns of M/C catalysts. Diffraction peaks of each metal and carbon are indicated by vertical colored bars and grey lines, respectively.

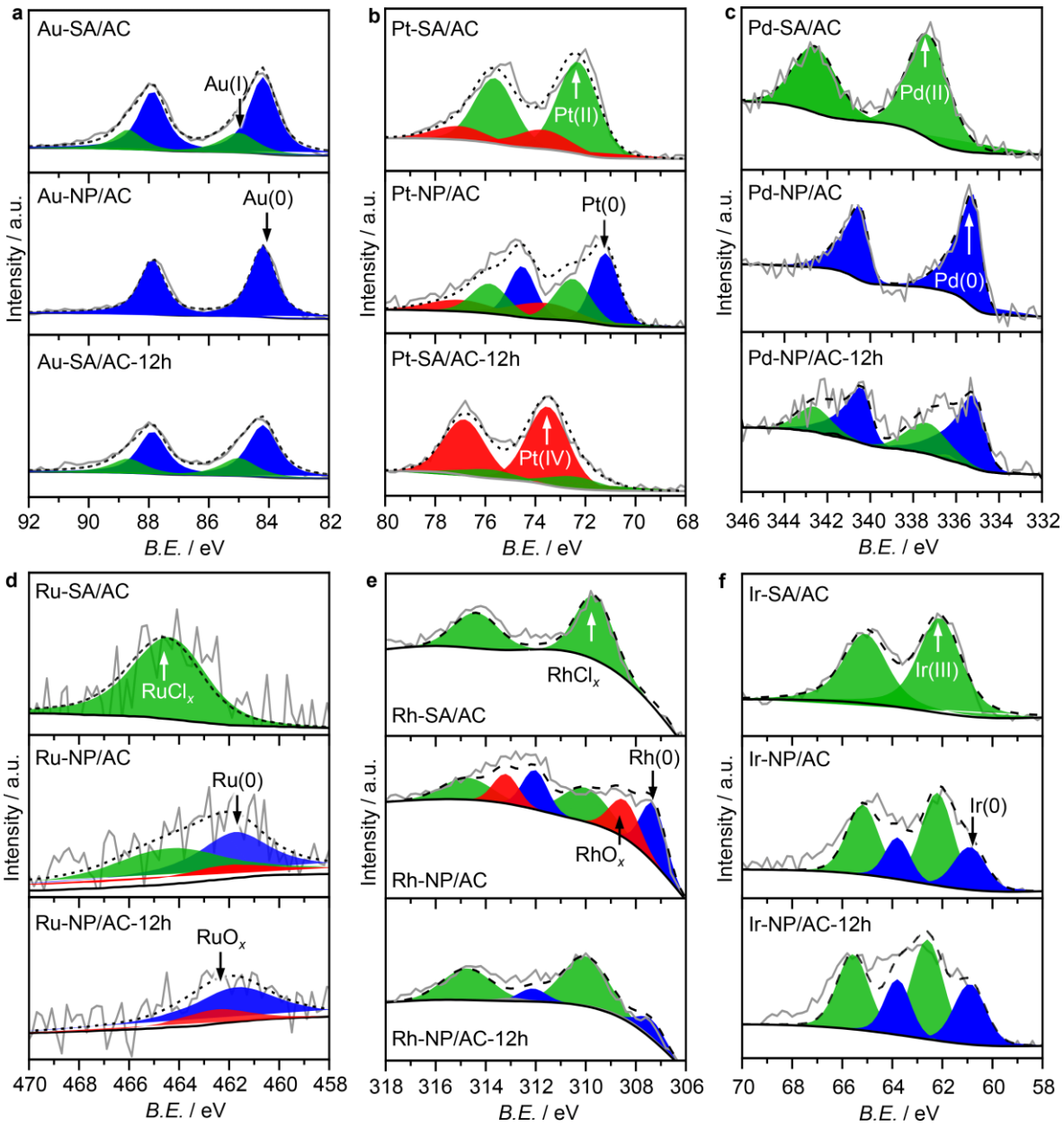

Supplementary Figure 4. Au 4*f*, Pt 4*f*, Pd 3*d*, Ru 3*p*, Rh 3*d*, and Ir 4*f* XPS spectra of fresh and used M/AC catalysts. Detailed fitting parameters are given in **Supplementary Table 2**. Notably, Au-Cl single atoms undergo photoreduction during XPS analysis, which results in a large contribution of Au(0) in the Au/C catalysts.[19]

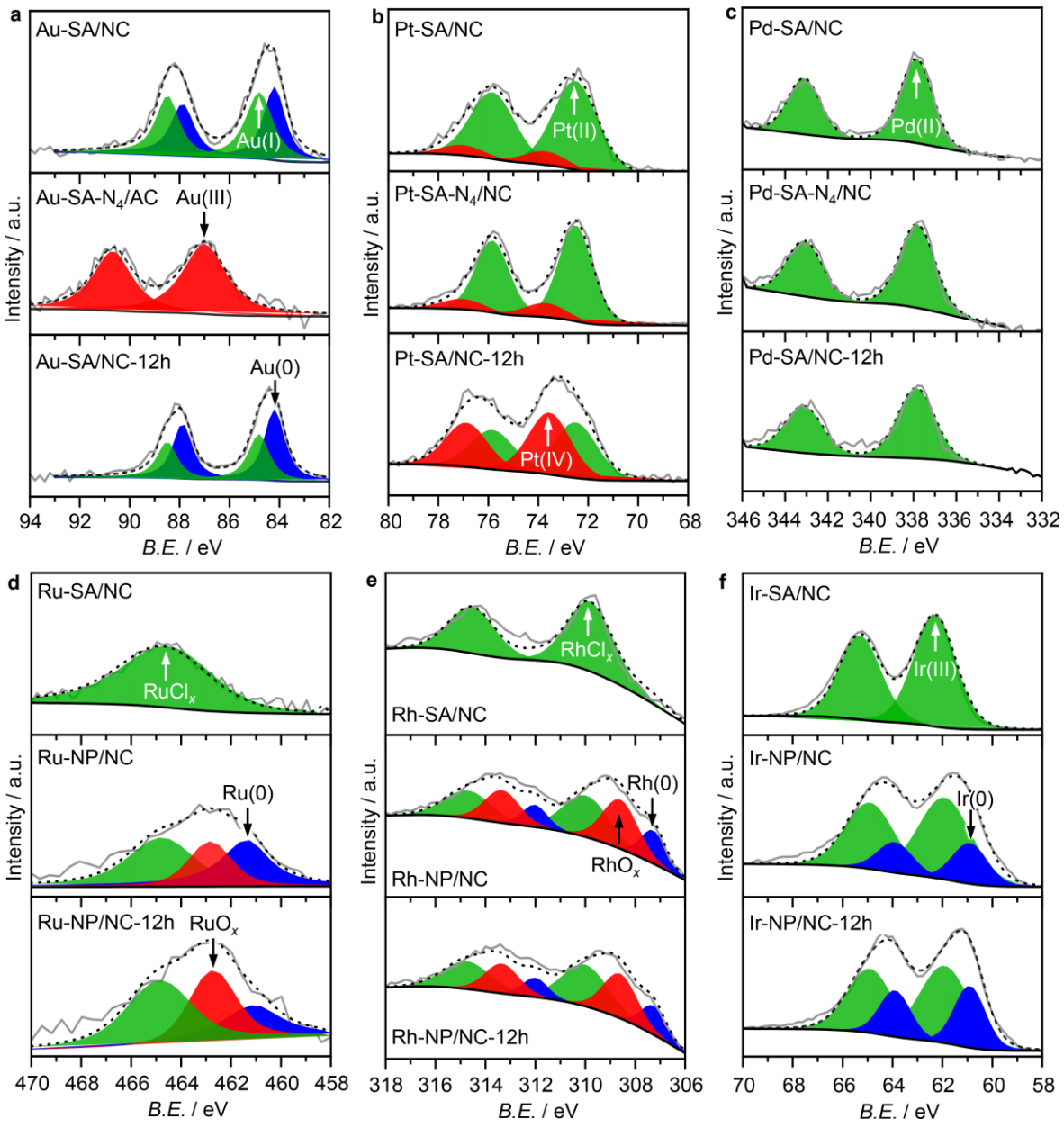

Supplementary Figure 5. Au 4*f*, Pt 4*f*, Pd 3*d*, Ru 3*p*, Rh 3*d*, and Ir 4*f* XPS spectra of fresh and used M/NC catalysts. Detailed fitting parameters are given in **Supplementary Table 2**. Notably, Au-Cl single atoms undergo photoreduction during XPS analysis, which results in a large contribution of Au(0) in the Au/C catalysts.[19]

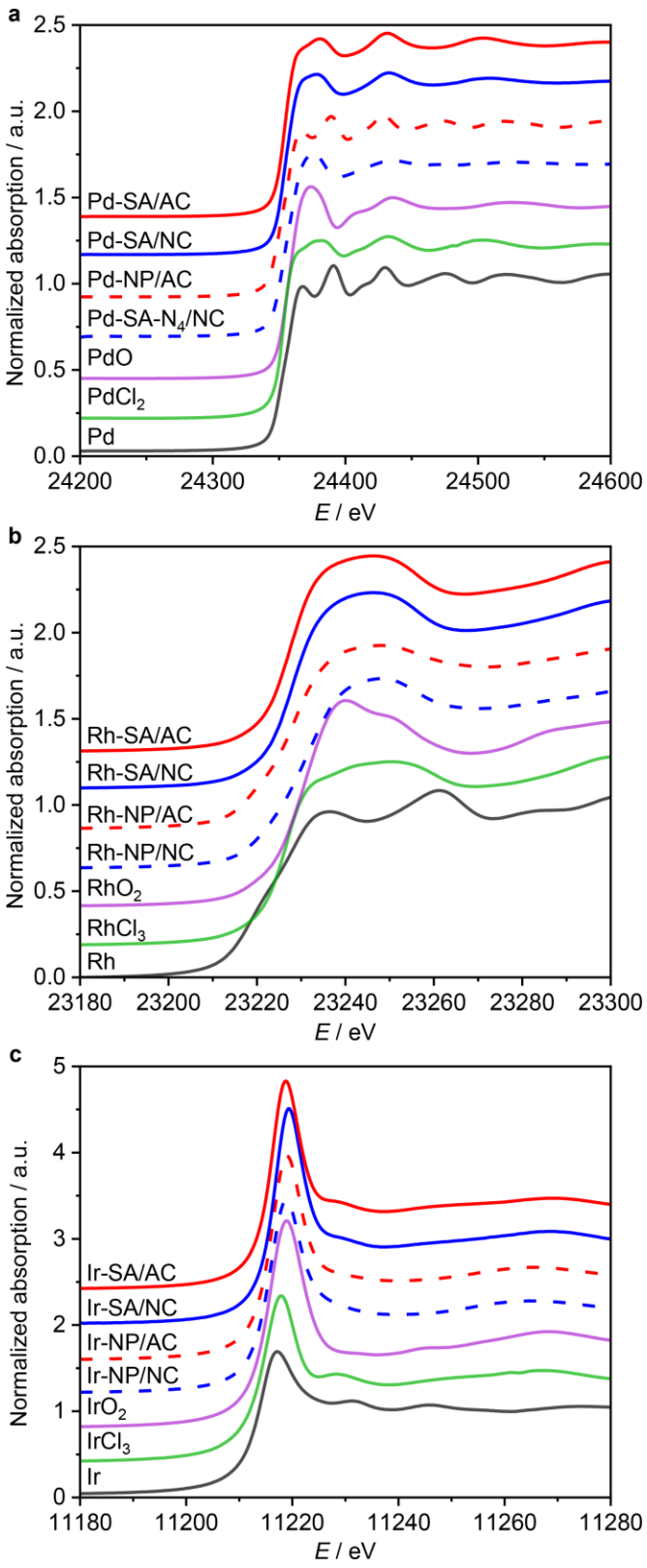

Supplementary Figure 6. XANES spectra of Pd/C, Rh/C, and Ir/C catalysts and reference materials at the Pd-*K*, Rh-*K*, and Ir-L_3 edges.

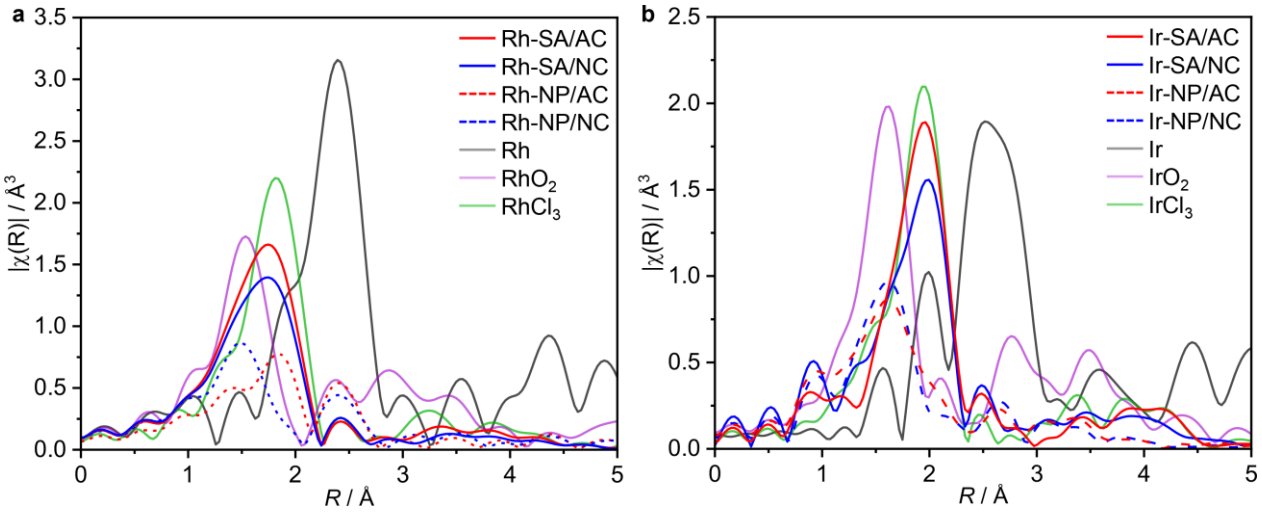

Supplementary Figure 7. EXAFS spectra of Rh/C and Ir/C catalysts and reference materials at the Rh-*K*, and Ir-L_3 edges.

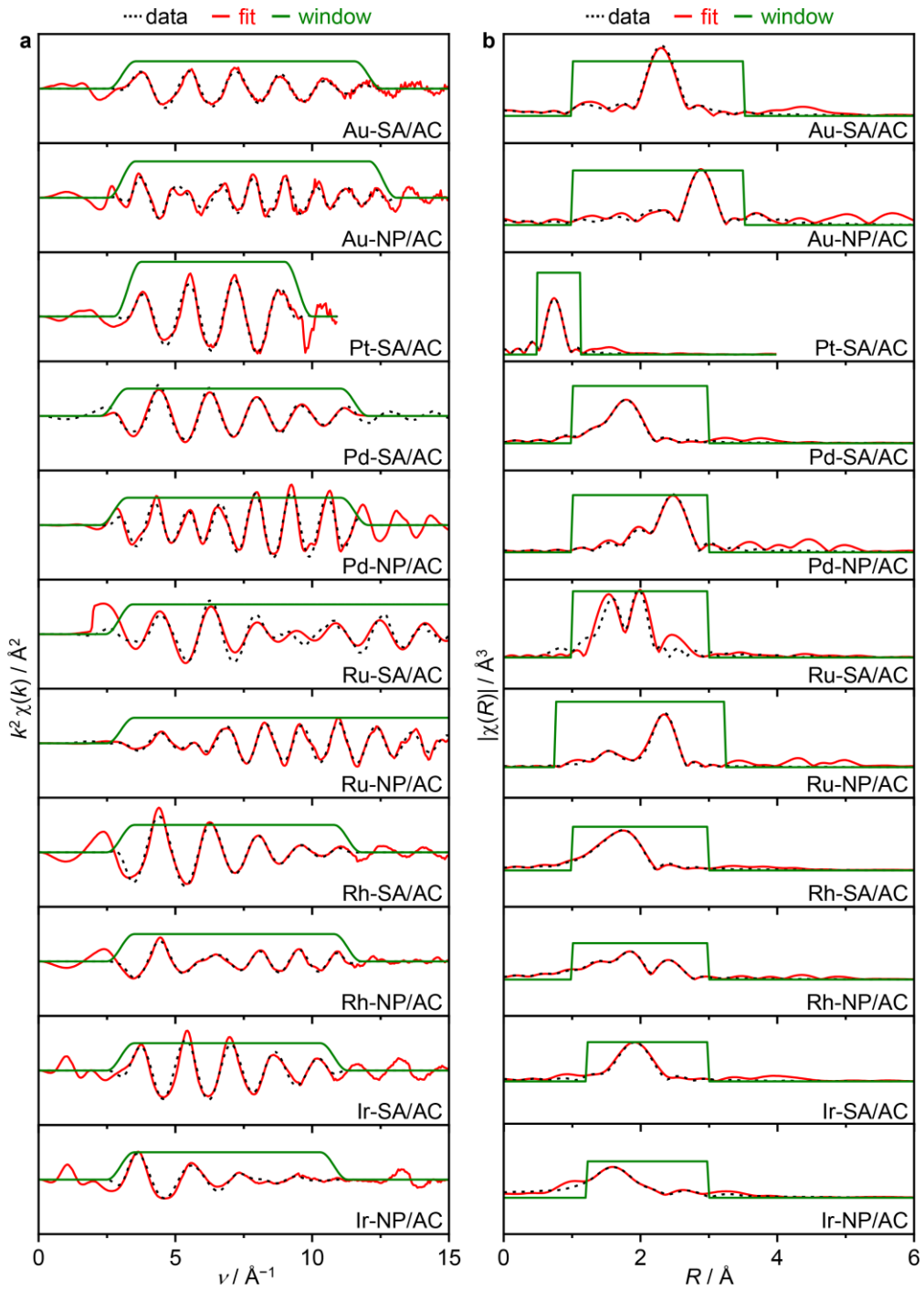

Supplementary Figure 8. Experimental and fitted EXAFS spectra of M/AC catalysts at the Au-L_3, Pt-L_3, Pd-*K*, Ru-*K*, Rh-*K* and Ir-L_3 edges. **a,** *k*-space. **b,** *R*-space. Fitting results are provided in **Supplementary Table 4**.

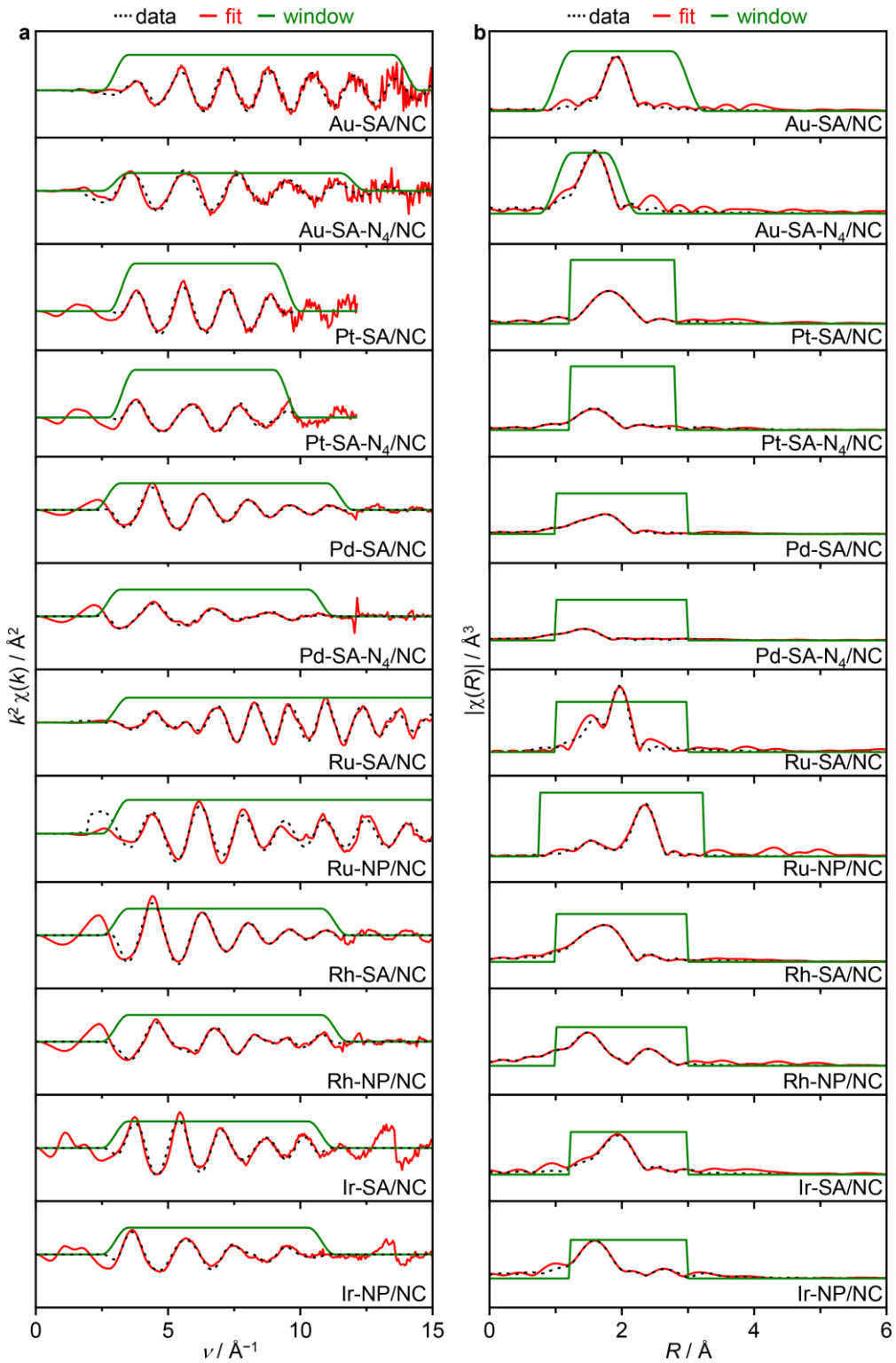

Supplementary Figure 9. Experimental and fitted EXAFS spectra of M/NC catalysts at the Au-L_3, Pt-L_3, Pd-*K*, Ru-*K*, Rh-*K*, and Ir-L_3 edges. **a,** *k*-space. **b,** *R*-space. Fitting results are provided in **Supplementary Table 5**.

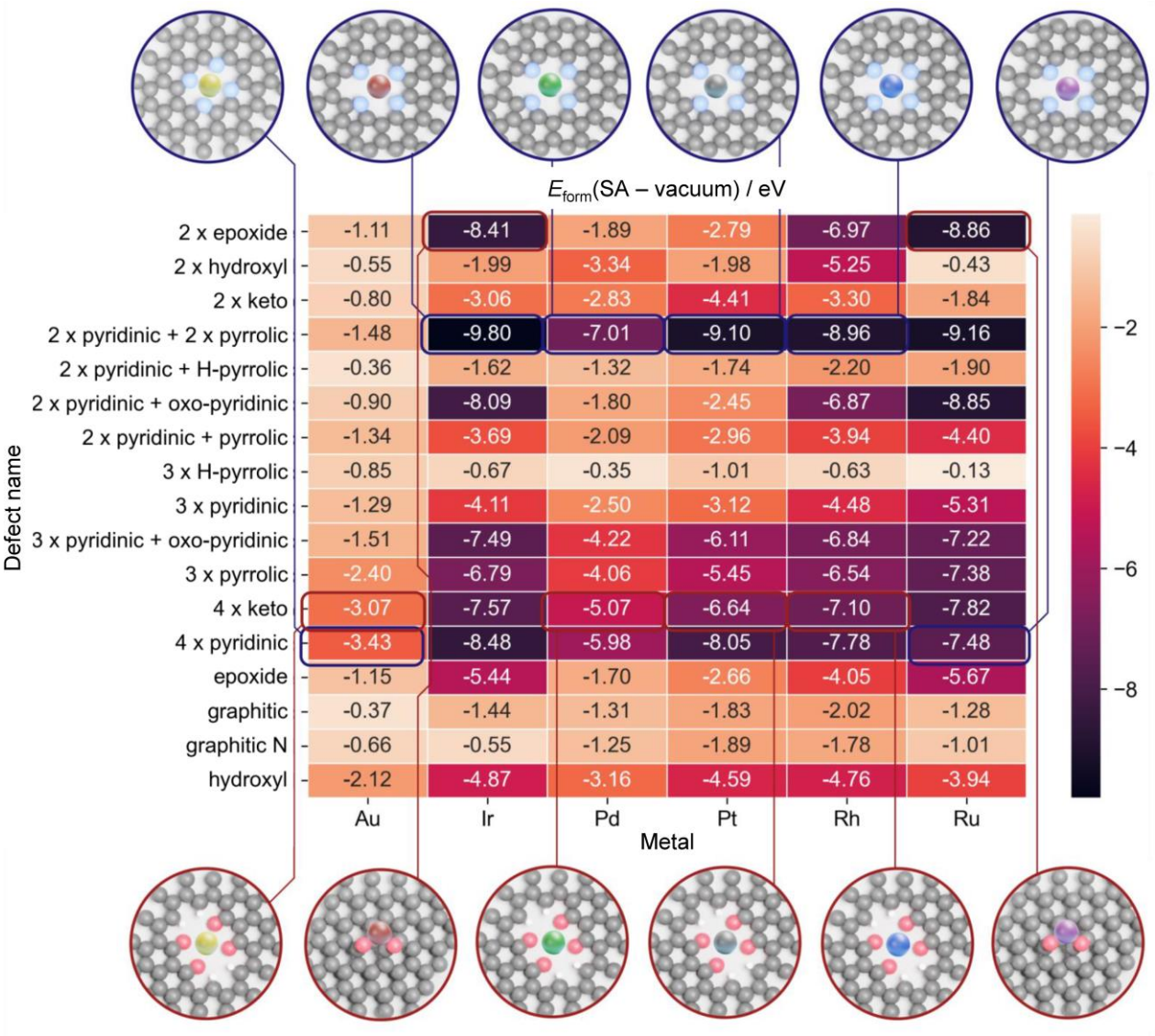

Supplementary Figure 10. Single-atom formation energy of Au, Pt, Pd, Ru, Rh and Ir single atoms over pristine graphite, NC (pyrrolic, pyridinic, oxo-pyridinic) and AC (hydroxyl, epoxidic, keto). The single-atom formation energy is defined as the energy of the formed SA motif versus the isolated atom and an empty defect under DFT conditions. Most stable configurations are highlighted and the corresponding motifs are shown as insets. Besides the highly stable 4-fold coordinated defects, the most favorable sites are the bi-epoxidic (AC) and the tri-pyrrolic (NC).

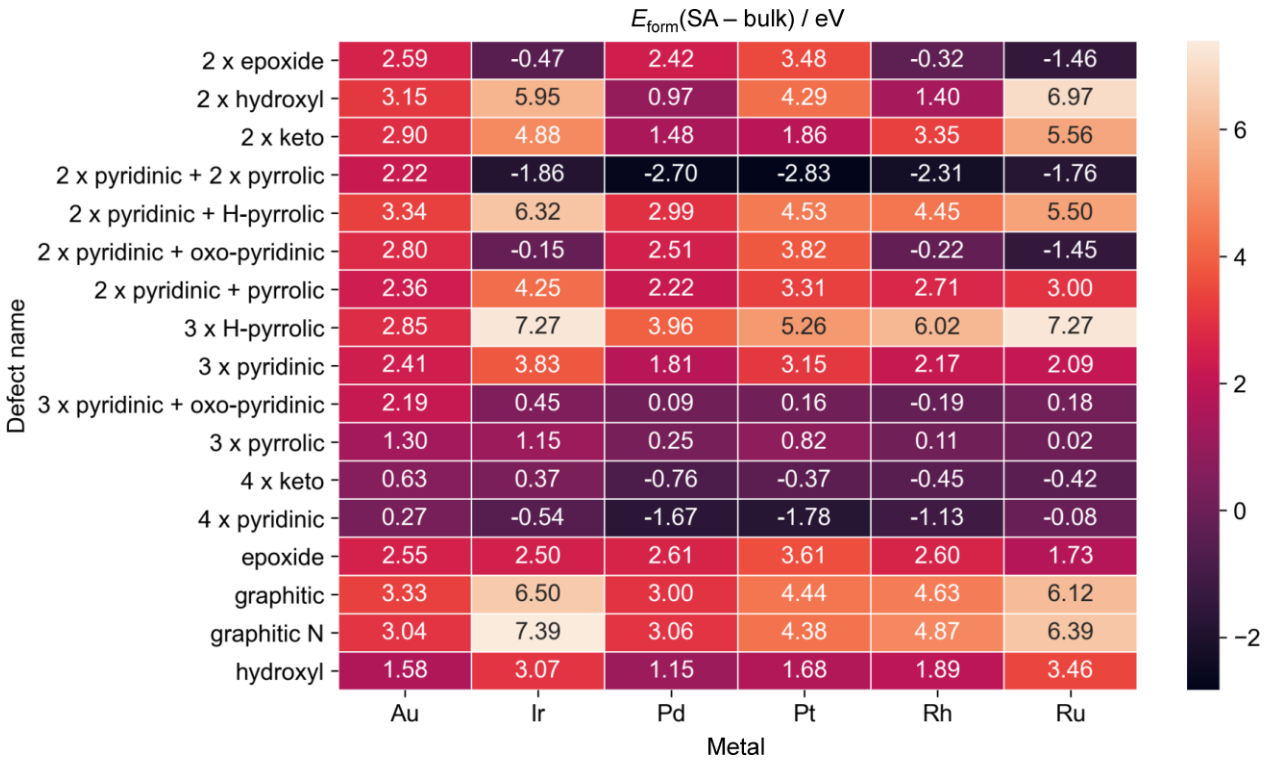

Supplementary Figure 11. Single-atom formation energy of Au, Pt, Pd, Ru, Rh and Ir single atoms over pristine graphite, NC (pyrrolic, pyridinic, oxo-pyridinic) and AC (hydroxyl, epoxidic). The single-atom formation energy is defined as the energy of the formed SA motif versus an atom in the metallic bulk and an empty defect. Besides the highly stable 4-fold coordinated defects, the most favorable sites are the bi-epoxidic (AC) and the tri-pyrrolic (NC).

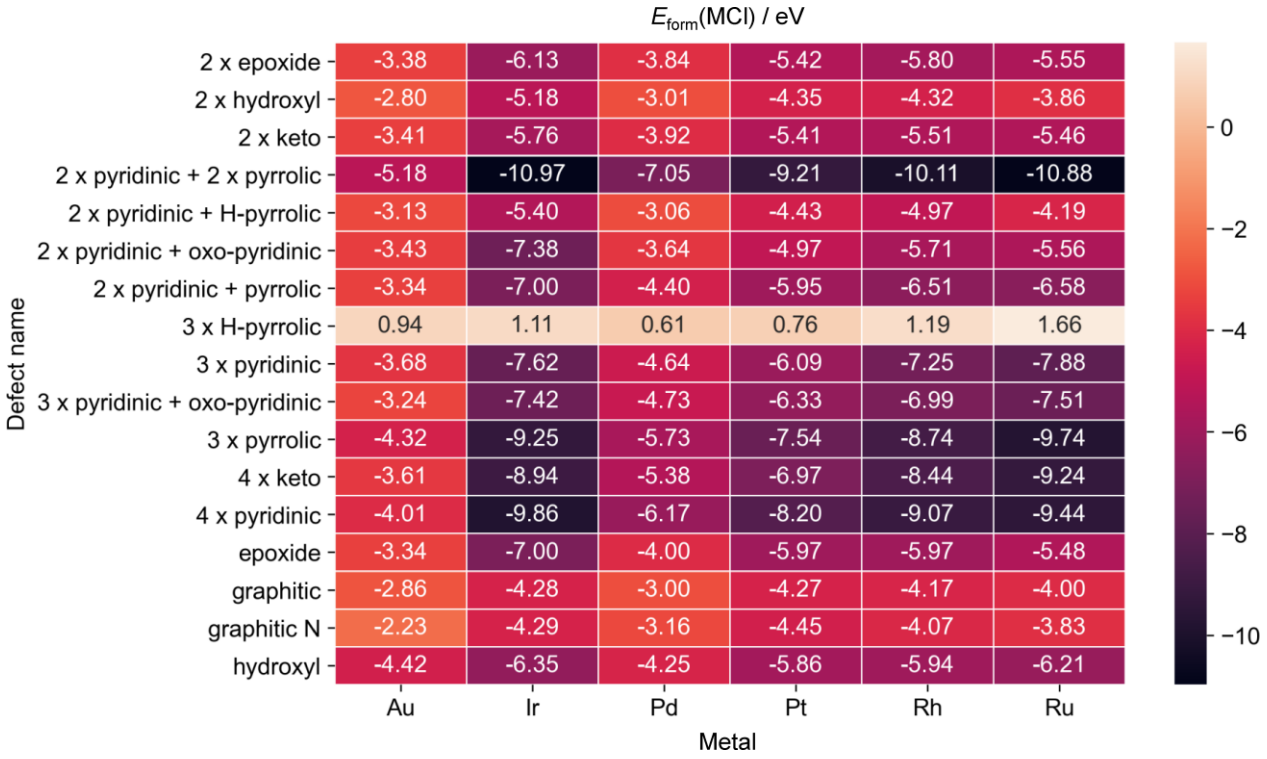

Supplementary Figure 12. MCl formation energy of Au, Pt, Pd, Ru, Rh and Ir MCl species over pristine graphite, NC (pyrrolic, pyridinic, oxo-pyridinic) and AC (hydroxyl, epoxidic, keto). The MCl formation energy is defined as the energy of the formed MCl motif versus an isolated M atom, ½ of an isolated Cl_2 molecule, and an empty defect.

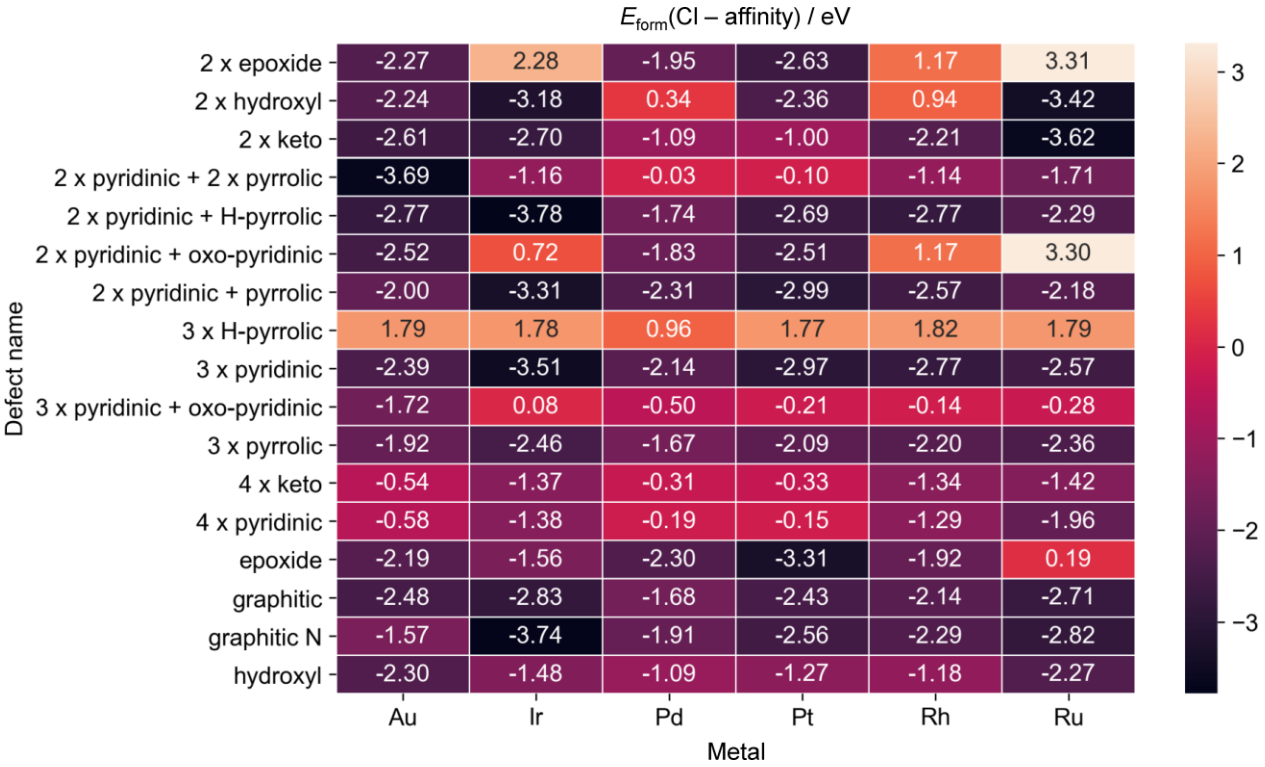

Supplementary Figure 13. Cl affinity of Au, Pt, Pd, Ru, Rh and Ir SA species formed over pristine graphite, NC (pyrrolic, pyridinic, oxo-pyridinic) and AC (hydroxyl, epoxidic, keto). Cl affinity is defined as the energy of the formed MCl motif versus a formed SA species and ½ of an isolated Cl_2 molecule.

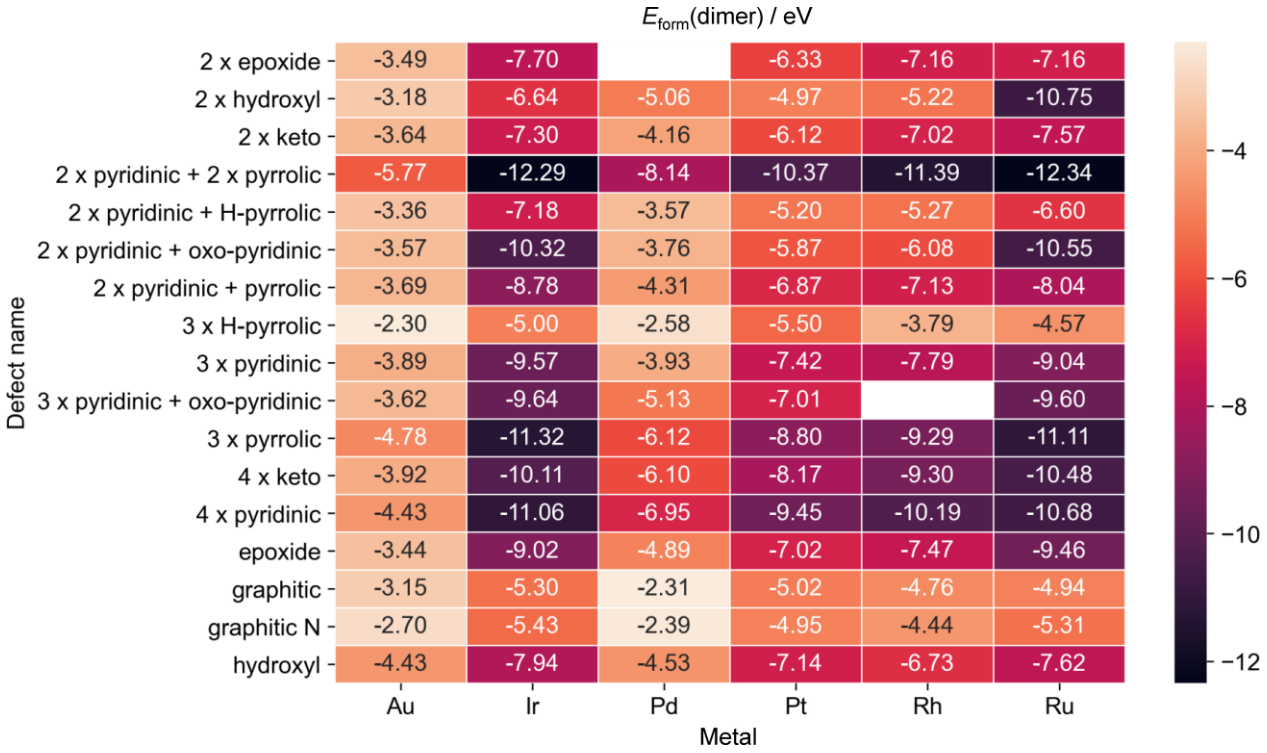

Supplementary Figure 14. Isolated dimer formation energy of Au, Pt, Pd, Ru, Rh and Ir over pristine graphite, NC (pyrrolic, pyridinic, oxo-pyridinic) and AC (hydroxyl, epoxidic, keto). The isolated dimer formation energy is defined as the energy of the formed dimer motif versus two isolated atoms and an empty defect.

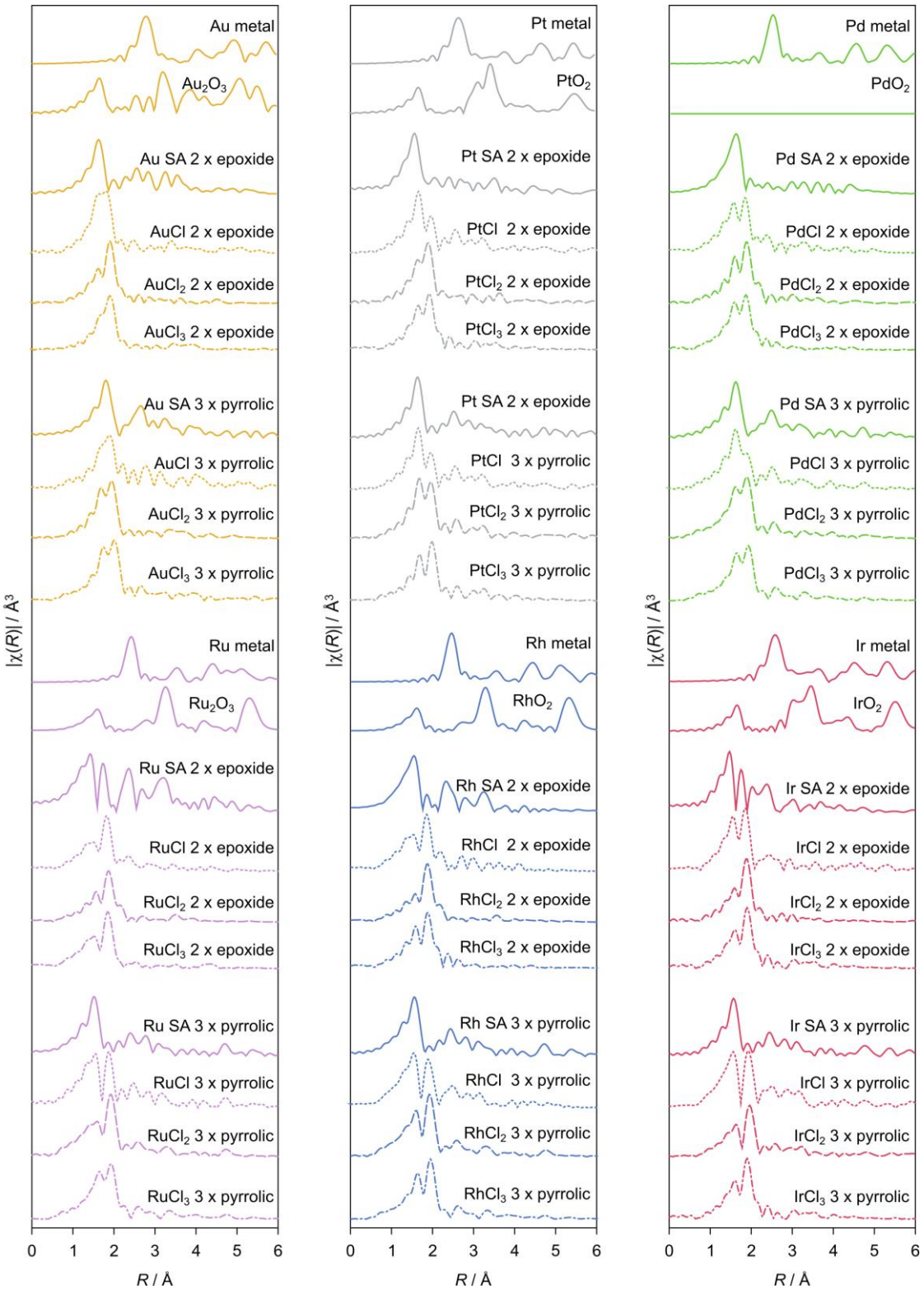

Supplementary Figure 15. Simulated EXAFS curves plotted in *R* space of the computationally obtained structures of metallic, oxidic, single atom and supported MCl_x species, for the examined set of metals (Au, Pt, Pd, Ru, Rh, Ir,).

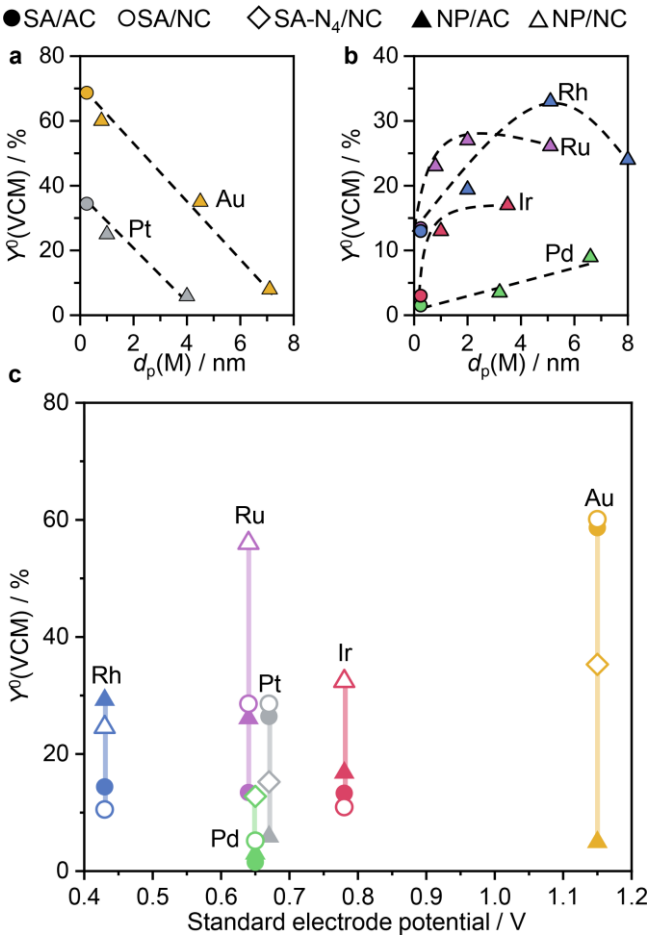

Supplementary Figure 16. Initial activity of M/C catalysts, expressed as the yield of vinyl chloride monomer, as a function of **a, b,** the mean metal particle size and **c,** the standard electrode potential of the respective metal chloride.[35]

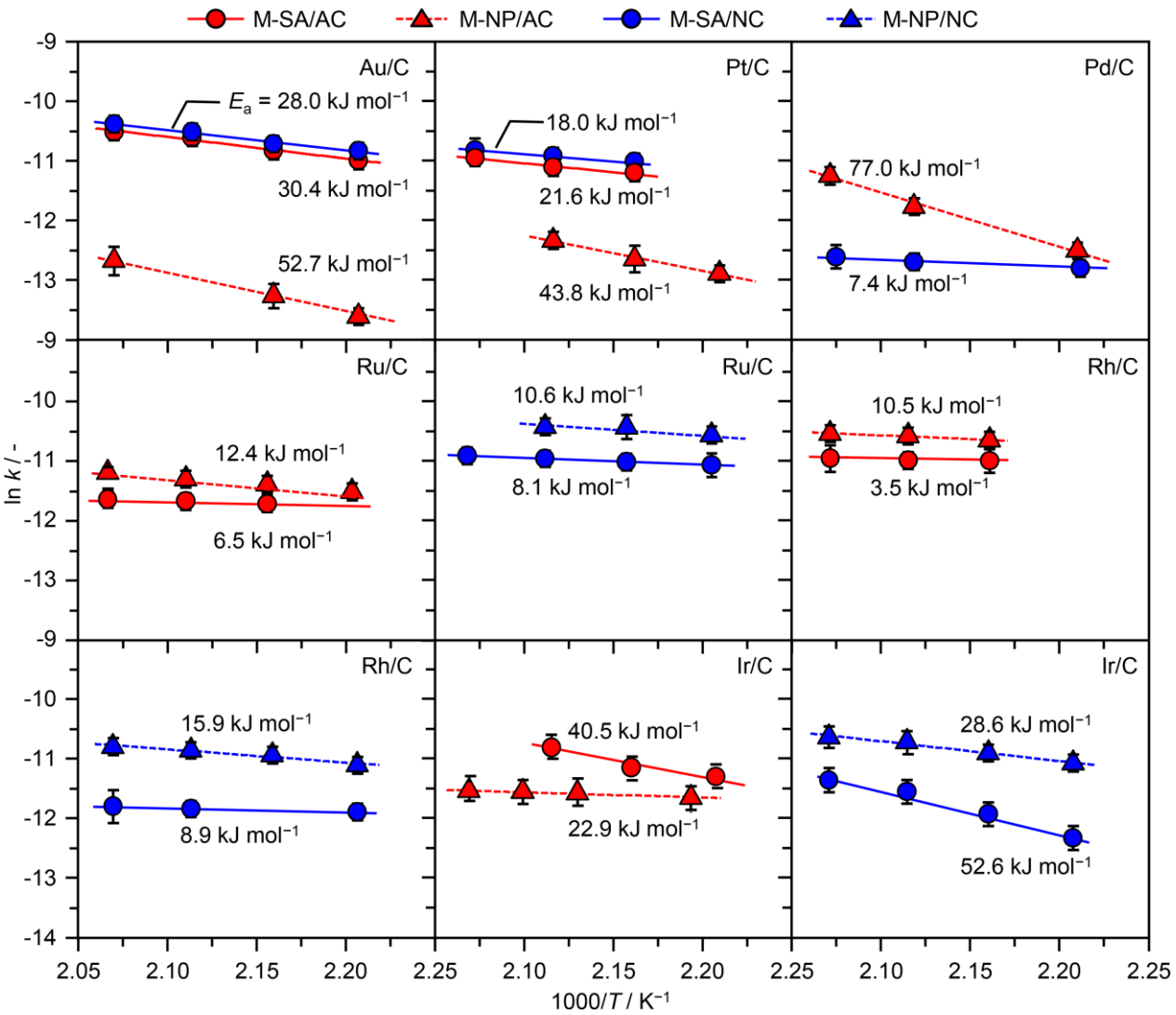

Supplementary Figure 17. Arrhenius plots of M/C catalysts in acetylene hydrochlorination with the corresponding apparent activation energy, E_a. Reaction conditions: T_{bed} = 473 K, F_T = 15 cm^3 min^{-1}, *GHSV*(C_2H_2) = 1500 h^{-1}, W_{cat} = 0.1 g, and P = 1 bar. In order to mitigate the influence of catalyst deactivation, each point was obtained in a single experiment, after 15 min *tos*.

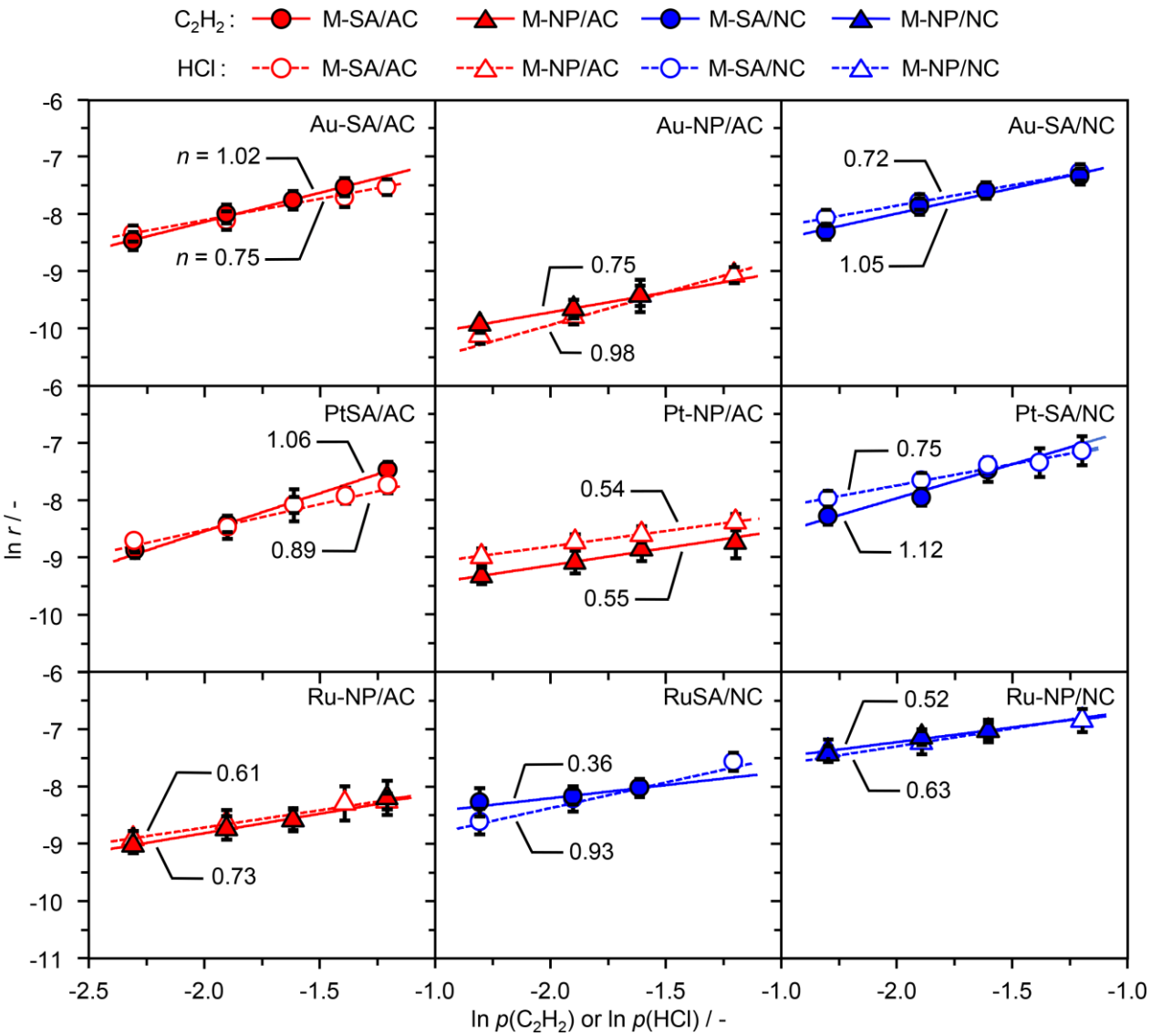

Supplementary Figure 18. Reaction rates, *r*, in acetylene hydrochlorination as a function of the inlet partial pressure of C_2H_2 or HCl. The partial reaction order of both reactants, *n*, is indicated by the slope of the solid and dashed fitting lines, respectively. Reaction conditions: T_{bed} = 473 K, F_T = 20 cm^3 min^{-1}, $p(C_2H_2,\ HCl)$ = 0.1-0.3 bar, W_{cat} = 0.1 g, and P = 1 bar. In order to mitigate the influence of catalyst deactivation, each point was obtained in a single experiment after 15 min *tos*.

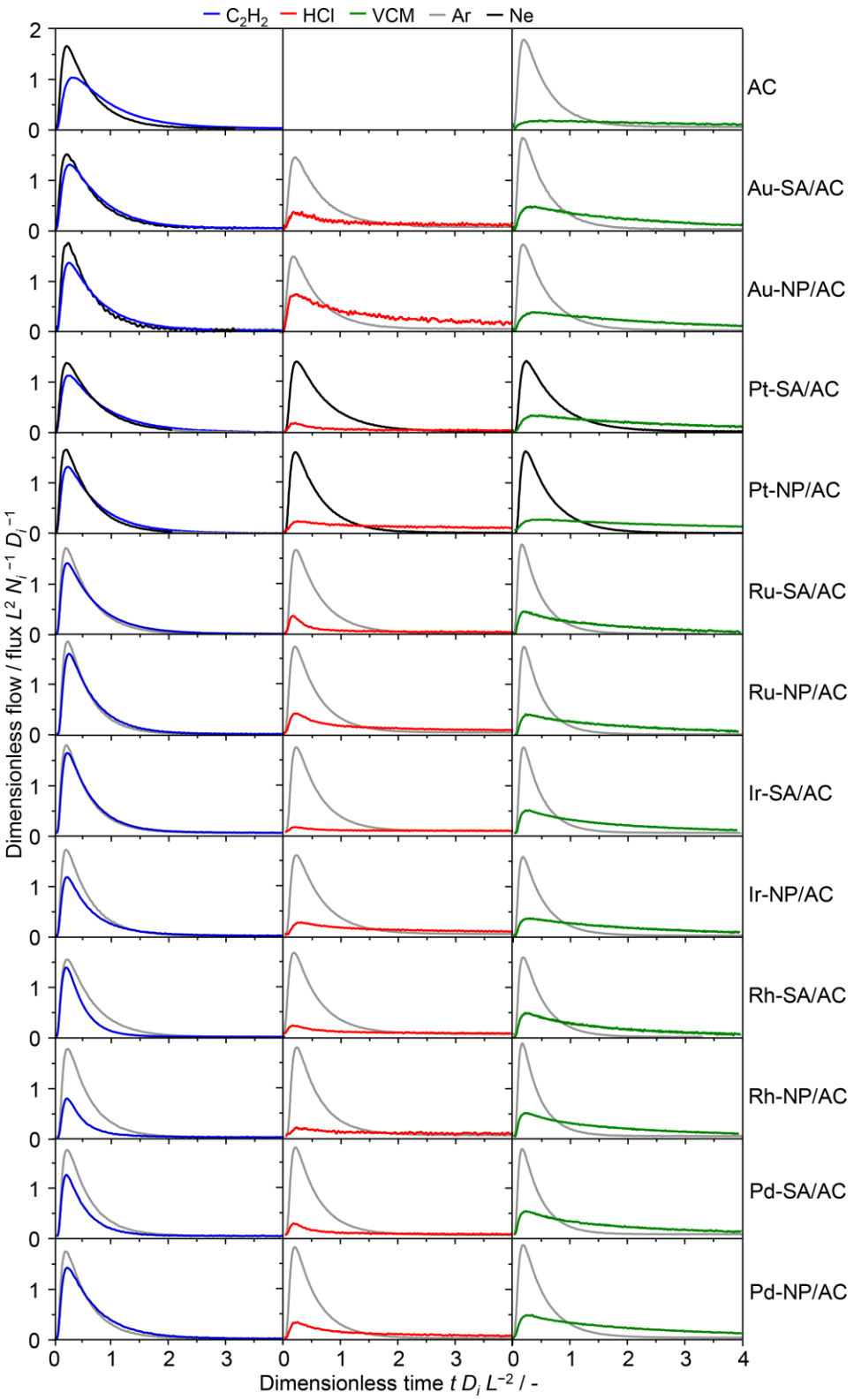

Supplementary Figure 19. Transient responses of reactive (C_2H_2, HCl, and VCM), and inert gases (Ne or Ar) upon single pulsing of C_2H_2:Ne (or Ar) = 1:1, HCl:Ne (or Ar) = 1:1, and VCM:Ne (or Ar) = 1:1, respectively, at 473 K over M/AC catalysts. HCl adsorbed irreversibly or was consumed over the AC support, as no response signal was detected at the reactor outlet (empty box).

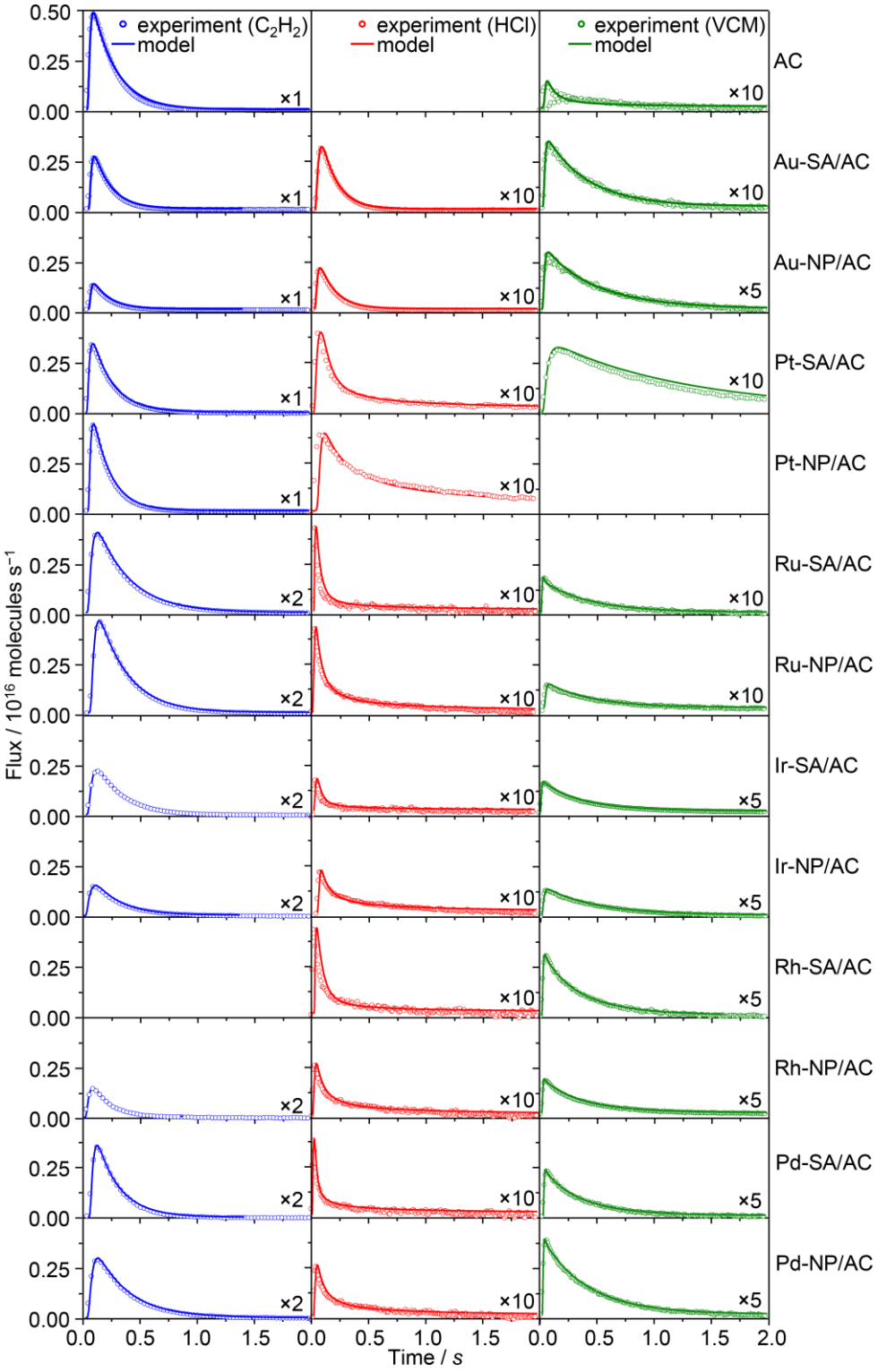

Supplementary Figure 20. Comparison between experimental and simulated responses of C_2H_2, HCl, and VCM over M/AC catalysts (**Supplementary Figure 19**). The adsorption and desorption constants are given in **Supplementary Table 8**. For AC and Pt-NP/AC no fitting procedure could be applied due to the irreversible adsorption or consumption of HCl and an unsatisfying fitting result, respectively (empty boxes).

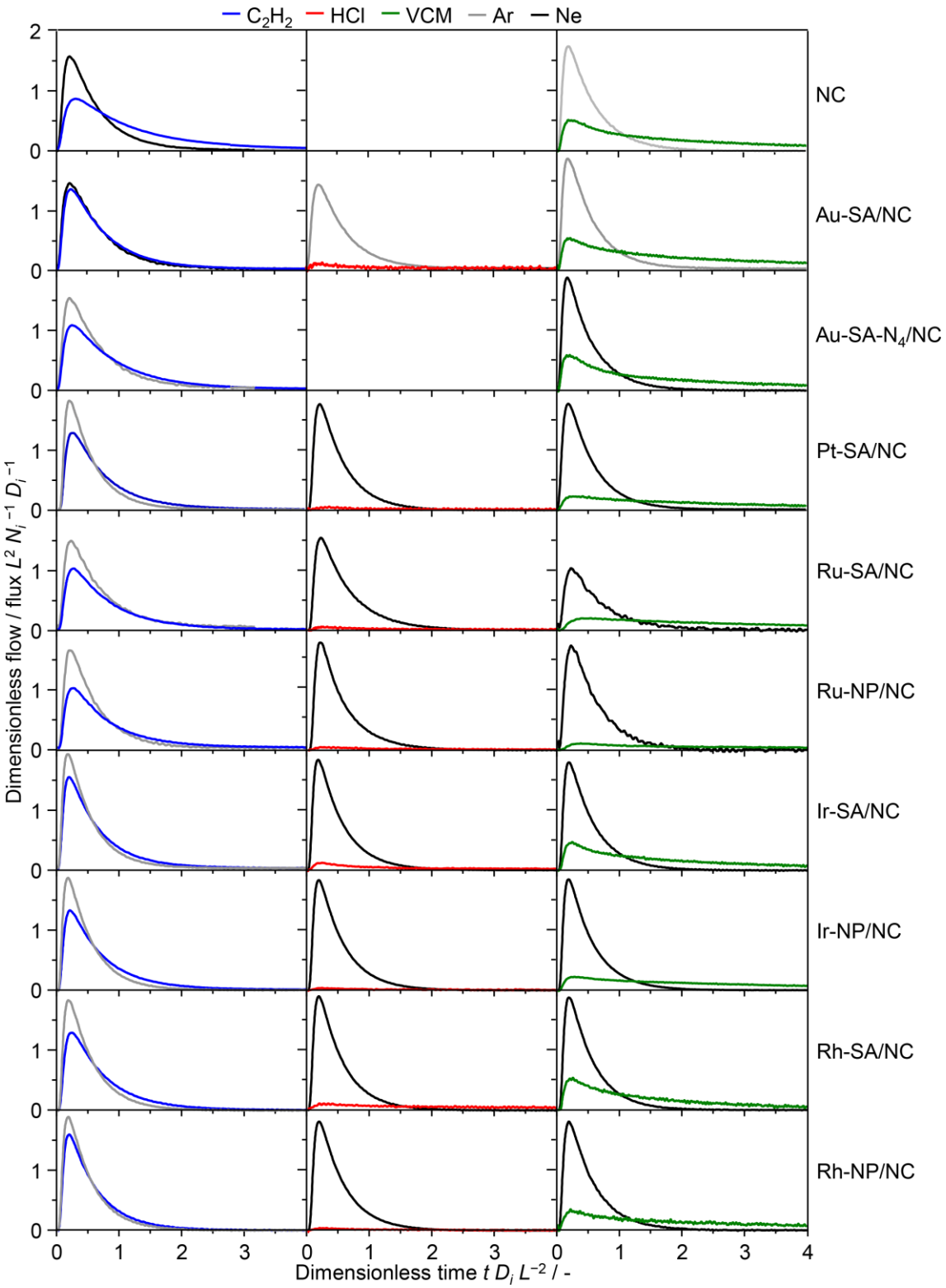

Supplementary Figure 21. Transient responses of reactive (C_2H_2, HCl, and VCM), and inert gases (Ne or Ar) upon single pulsing of C_2H_2:Ne (or Ar) = 1:1, HCl:Ne (or Ar) = 1:1, and VCM:Ne (or Ar) = 1:1, respectively, at 473 K over M/NC catalysts. Empty boxes indicate that HCl adsorbed irreversibly or was consumed, as no response signal was detected at the reactor outlet.

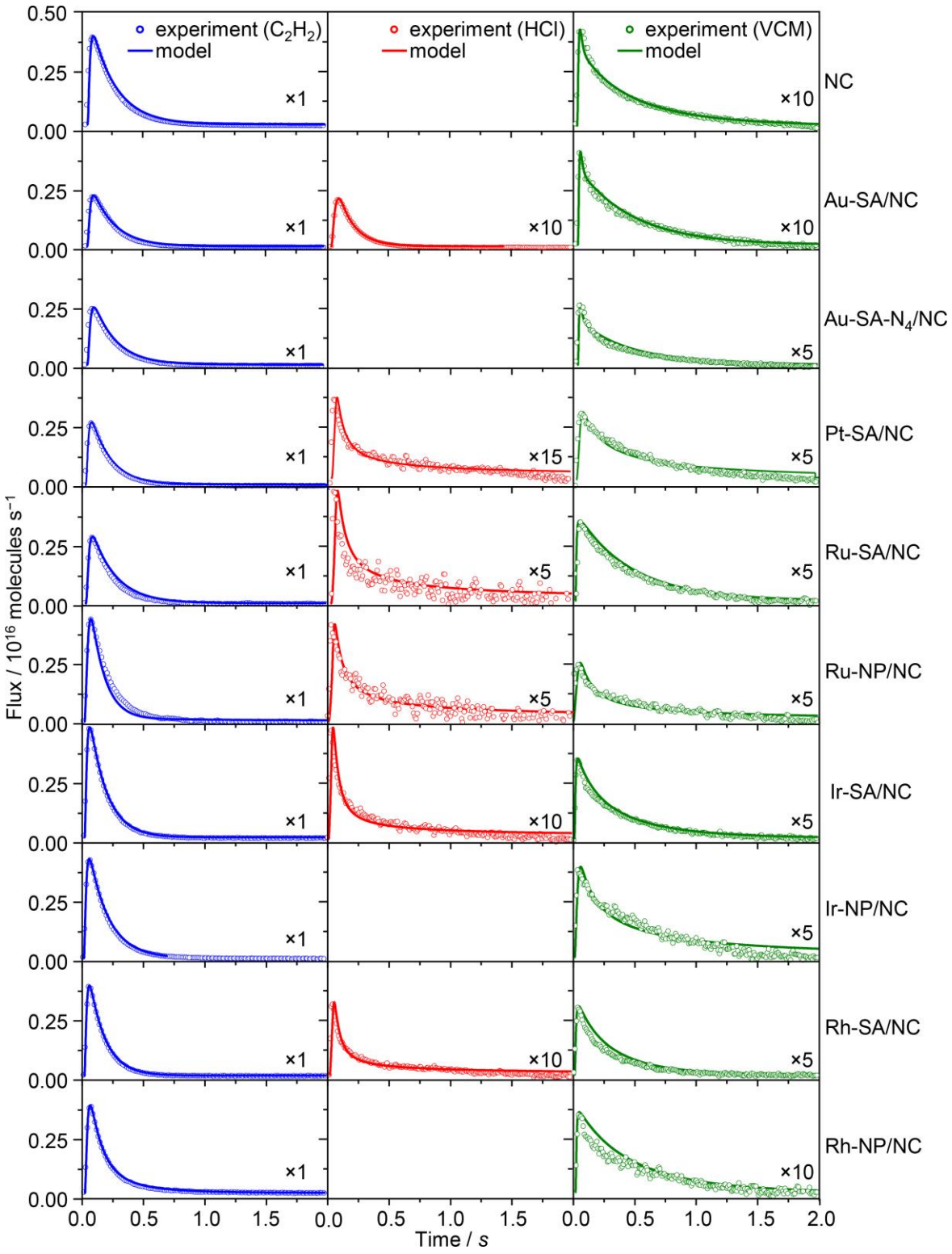

Supplementary Figure 22. Comparison between experimental and simulated responses of C_2H_2, HCl, and VCM over M/NC catalysts (**Supplementary Figure 21**). The adsorption and desorption constants are given in **Supplementary Table 8**. For NC, Au-SA-N_4/NC, Ir-NP/NC, and Rh-NP/NC no fitting procedure could be applied due to the irreversible adsorption or consumption of HCl (empty boxes).

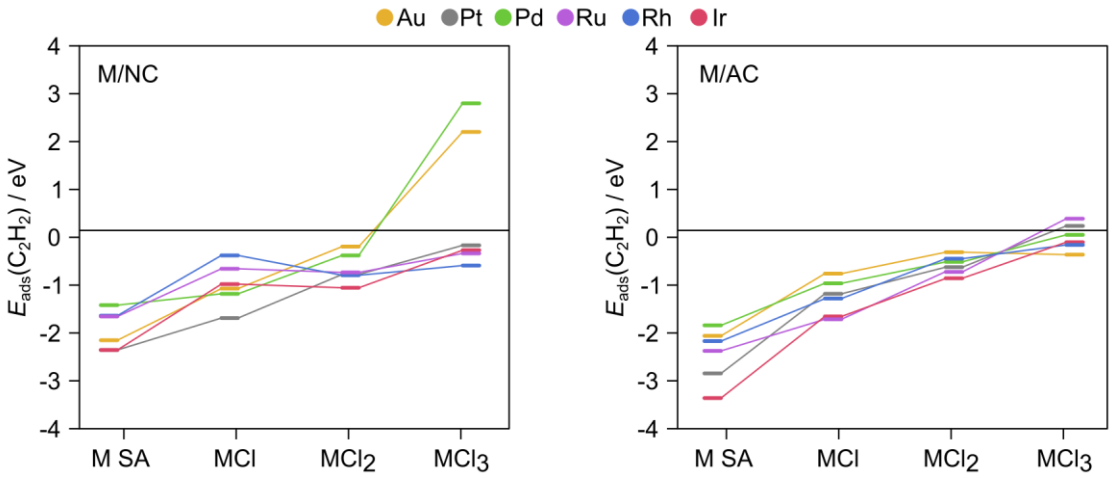

Supplementary Figure 23. Adsorption energy of acetylene over single-atoms species with varying number of Cl ligands in their coordination spheres.

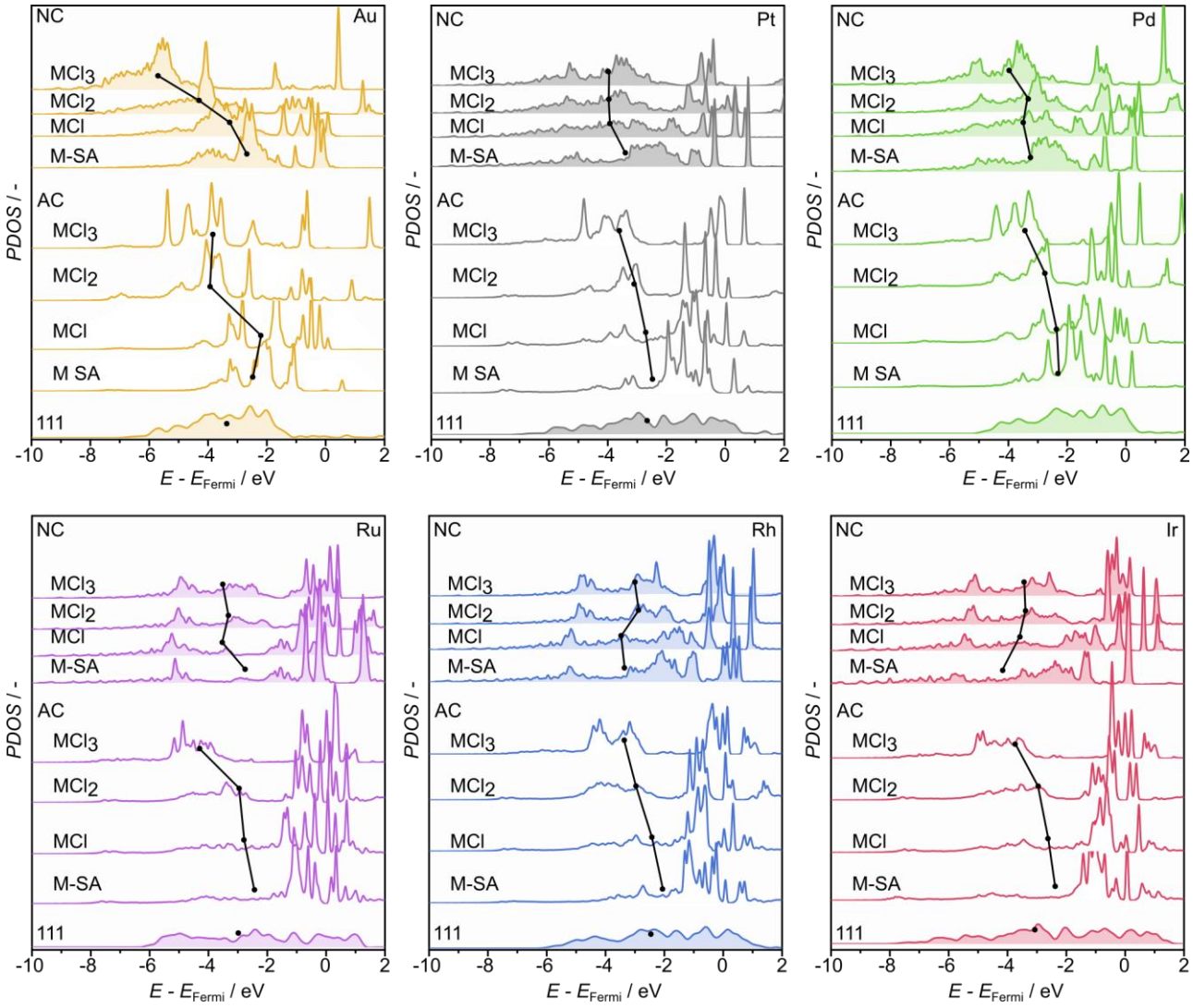

Supplementary Figure 24. Projected density of *d*-states for single-atom species (M-SA, MCl, MCl_2, MCl_3) and the (111) metal surfaces. The band centers are represented by black circles.

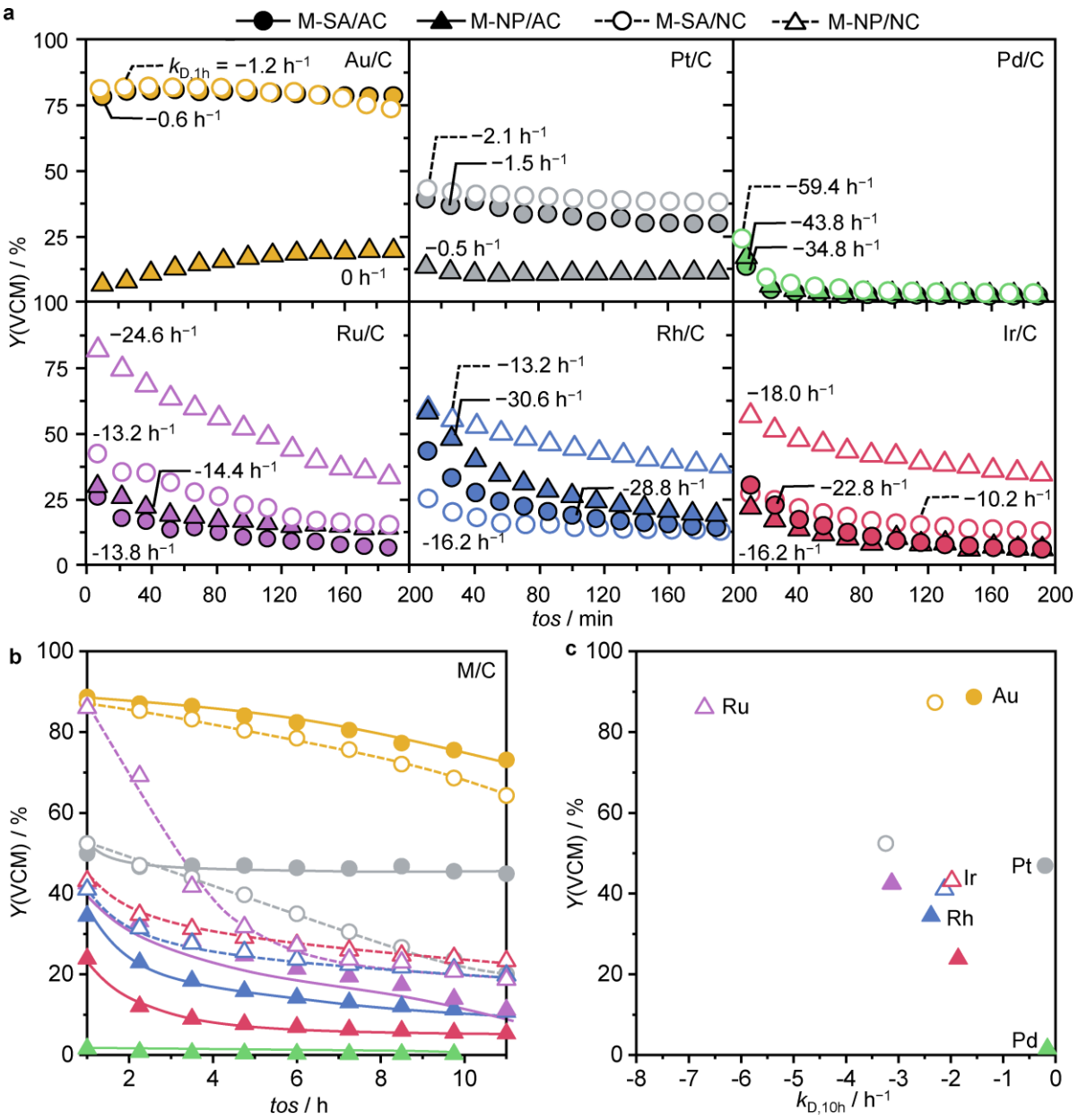

Supplementary Figure 25. Stability tests of M/C catalysts in acetylene hydrochlorination for **a,** 3 h *tos* and **b,** 12 h *tos* with respective deactivation constants k_D. **c,** Overview of the initial activities, represented as the yield of vinyl chloride, Y^0(VCM), and the stability of M/C catalysts, as indicated by their deactivation constants **Supplementary Table 1**).

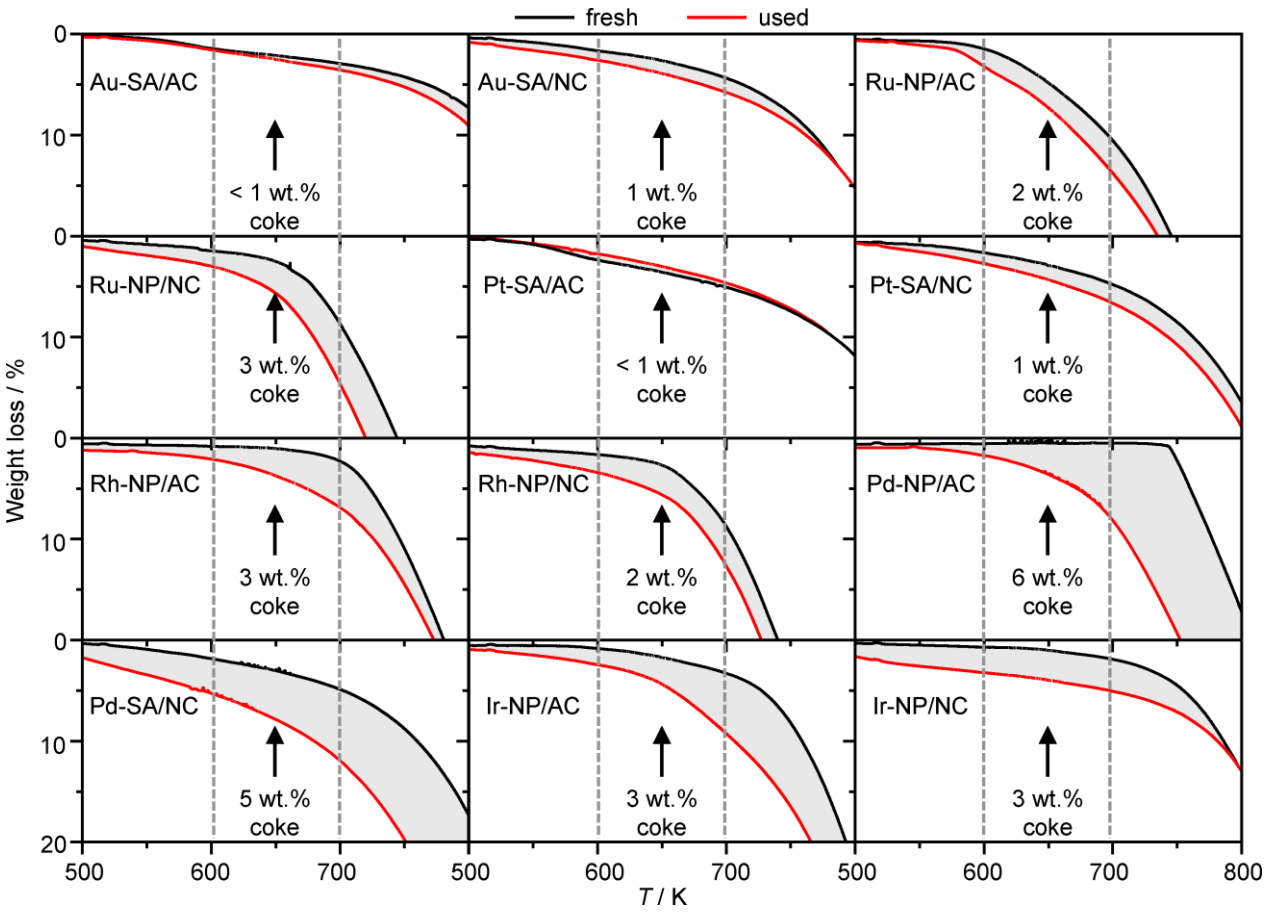

Supplementary Figure 26. TGA in 20 vol.% O_2/Ar of fresh catalysts (black lines) and after use in acetylene hydrochlorination for 3 h, respectively (red lines). The difference in weight-loss between the fresh and used samples is highlighted by the grey colored area. Quantification of coke in the used samples was assessed by integrating each TGA profile in reference to the as-prepared sample in the temperature region of 600-700 K.

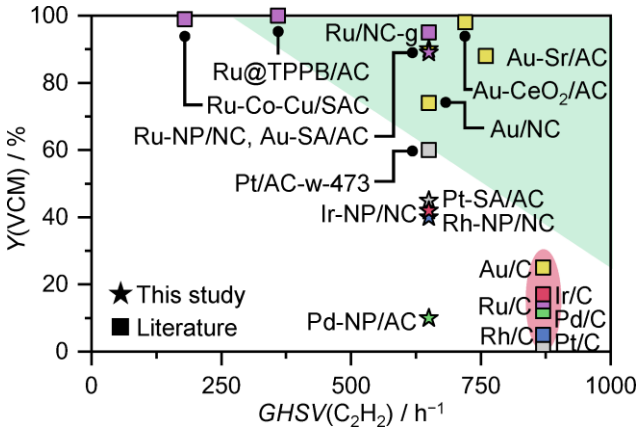

Supplementary Figure 27. Performance in acetylene hydrochlorination, indicated by the yield of vinyl chloride monomer achieved at respective gas hourly space velocities, of selected catalysts developed in this study (star symbols) in comparison to previous screening studies (red colored area) and state-of-the art systems (green colored area). Individual reaction conditions are provided in **Supplementary Table 10**.

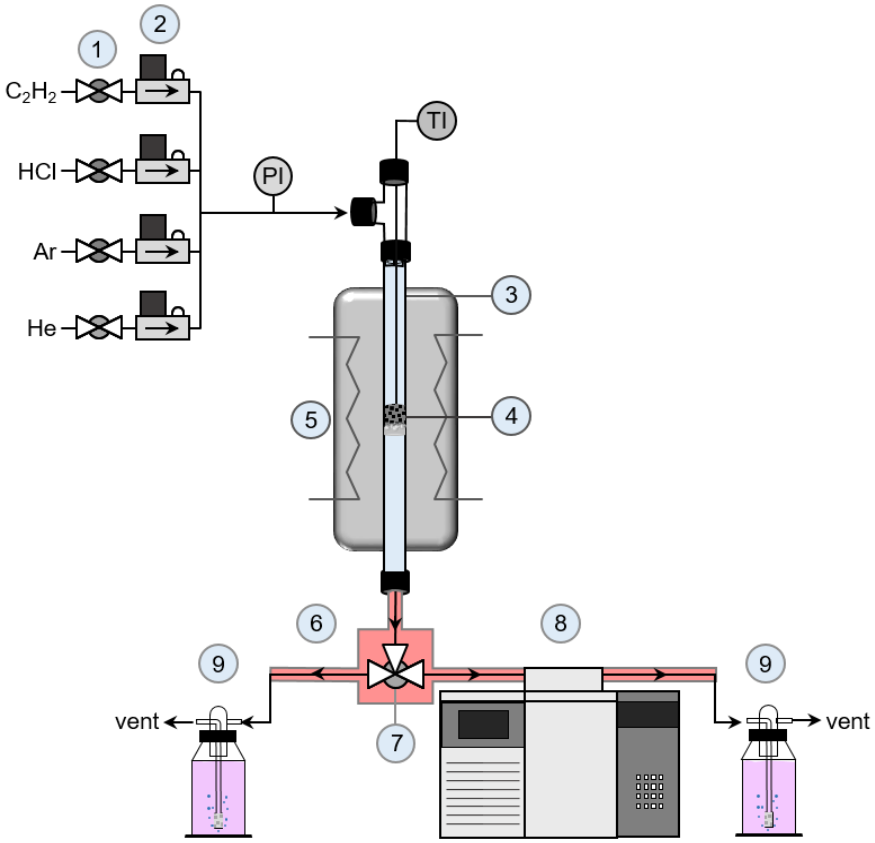

Supplementary Figure 28. Scheme of the laboratory set-up used for acetylene hydrochlorination. 1: two-way on-off valves, 2: mass-flow controllers, 3: quartz reactor, 4: catalyst bed, 5: oven, 6: heat tracing (red coloring), 7: three-way sampling valve, 8: gas chromatograph connected to a mass spectrometer, 9: NaOH scrubbers, PI: pressure indicator, and TI: temperature indicator.

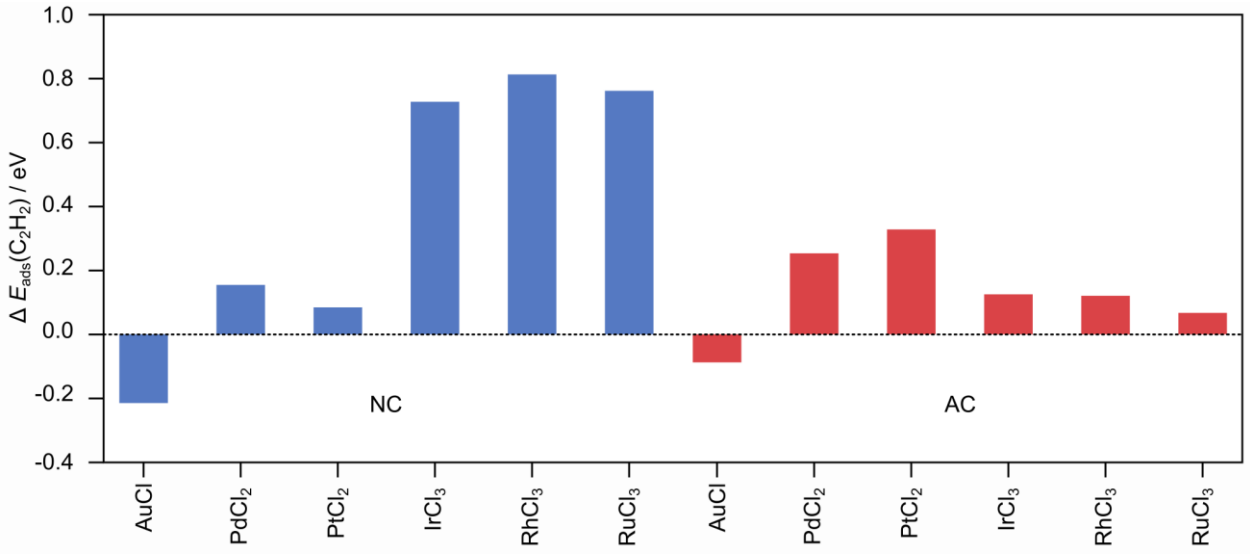

Supplementary Figure 29. Differences between the acetylene adsorption energy over M/AC (M in bi-epoxidic defect) and M/NC (M in tri-pyrrolic defect) before and after replacing one of the N/O atoms in the primary metal coordination sphere with a C atom. The difference in adsorption energies is defined as $\Delta E_{ads}(C_2H_2) = E_{ads,N/O}(C_2H_2) - E_{ads,C}(C_2H_2)$. In order to prevent defect reconstruction induced by the change in the heteroatom defect species, the geometry of the defect was kept constant during ionic relaxation.

References

1 Lin, R., Kaiser, S. K., Hauert, R. & Pérez-Ramírez, J. Descriptors for high-performance nitrogen-doped carbon catalysts in acetylene hydrochlorination. *ACS Catal.* **8**, 1114-1121 (2018).

2 Abdala, P. M. *et al.* Scientific opportunities for heterogeneous catalysis research at the SuperXAS and SNBL beam lines. *Chimia* **66**, 699-705 (2012).

3 Muller, O., Nachtegaal, M., Just, J., Lutzenkirchen-Hecht, D. & Frahm, R. Quick-EXAFS setup at the SuperXAS beamline for *in situ* X-ray absorption spectroscopy with 10 ms time resolution. *J. Synchrotron Radiat.* **23**, 260-266 (2016).

4 Clark, A. H., Imbao, J., Frahm, R. & Nachtegaal, M. ProQEXAFS: A highly optimized parallelized rapid processing software for QEXAFS data. *J. Synchrotron Radiat.* **27**, 551-557 (2020).

5 Newville, M. IFEFFIT: Interactive XAFS analysis and FEFF fitting. *J. Synchrotron Radiat.* **8**, 322-324 (2001).

6 Carberry, J. J. in *Catalysis: Science and Technology* (eds J.R. Anderson & M. Boudart) Ch. 3, 131-171 (Springer-Verlag, 1987).

7 Mears, D. Diagnostic criteria for heat transport limitations in fixed bed reactors. *J. Catal.* **20**, 127-131 (1971).

8 Weisz, P. B. & Prater, C. D. Interpretation of measurements in experimental catalysis. *Adv. Catal.* **6**, 143-196 (1954).

9 Gleaves, J. T., Yablonskii, G. S., Phanawadee, P. & Schuurman, Y. TAP-2: An interrogative kinetics approach. *Appl. Catal., A* **160**, 55-88 (1997).

10 Soick, M., Wolf, D. & Baerns, M. Determination of kinetic parameters for complex heterogeneous catalytic reactions by numerical evaluation of TAP experiments. *Chem. Eng. Sci.* **55**, 2875-2882 (2000).

11 Pérez-Ramírez, J. & Kondratenko, E. V. Evolution, achievements, and perspectives of the TAP technique. *Catal. Today* **121**, 160-169 (2007).

12 Baerns, M., Buyevskaya, O. V., Mleczko, L. & Wolf, D. Catalytic partial oxidation of methane to synthesis gas-catalysis and reaction engineering. *Stud. Surf. Sci. Catal.* **107**, 421-428 (1997).

13 W.H. Press, B.P. Flannery, S.A. Teukolsky & Vetterling, W. T. *Numerical Recipes in FORTRAN*. second ed. edn, (Cambridge University Press, 1992).

14 Kresse, G. & Furthmüller, J. Efficiency of ab-initio total energy calculations for metals and semiconductors using a plane-wave basis set. *Comput. Mater. Sci.* **6**, 15-50 (1996).

15 Perdew, J. P. *et al.* Atoms, molecules, solids, and surfaces: Applications of the generalized gradient approximation for exchange and correlation. *Phys. Rev. B* **46**, 6671-6687 (1992).

16 G. Kresse, D. J. From ultrasoft pseudopotentials to the projector augmented-wave method. *Phys. Rev. B* **59**, 1758-1775 (1999).

17 Grimme, S., Antony, J., Ehrlich, S. & Krieg, H. A consistent and accurate *ab initio* parametrization of density functional dispersion correction (DFT-D) for the 94 elements H-Pu. *J. Chem. Phys.* **132**, 154104 (2010).

18 Fako, E. *ioChem-BD Collection* (Institute of Chemical Research of Catalonia, accessed 17 March 2021); https://doi.org/10.19061/iochem-bd-1-204.

19 Kaiser, S. K. *et al.* Controlling the speciation and reactivity of carbon-supported gold nanostructures for catalysed acetylene hydrochlorination. *Chem. Sci.* **10**, 359-369 (2019).

20 Kaiser, S. K. *et al.* Nanostructuring unlocks high performance of platinum single-atom catalysts for stable vinyl chloride production. *Nat. Catal.* **3**, 376-385 (2020).

21 Brun, M., Berthet, A. & Bertolini, J. C. XPS, AES and Auger parameter of Pd and PdO. *J. Electron Spectros. Relat. Phenomena* **104**, 55-60 (1999).

22 Militello, M. C. & Simko, S. J. Palladium Chloride ($PdCl_2$) by XPS. *Surf. Sci. Spectra* **3**, 402-409 (1994).

23 Kaiser, S. K., Lin, R., Krumeich, F., Safonova, O. V. & Pérez-Ramírez, J. Preserved in a shell: high-performance graphene-confined ruthenium nanoparticles in acetylene hydrochlorination. *Angew. Chem. Int. Ed.* **58**, 12297-12304 (2019).

24 Kibis, L. S., Stadnichenko, A. I., Koscheev, S. V., Zaikovskii, V. I. & Boronin, A. I. XPS study of nanostructured rhodium oxide film comprising Rh^{4+} species. *J. Phys. Chem. C* **120**, 19142-19150 (2016).

25 Muñoz, A., Munuera, G., Malet, P., González-Elipe, A. R. & Espinós, J. P. XPS and TRP/TPO study of the behaviour of rhodium particles supported on TiO_2. *Surf. Interface Anal.* **12**, 247-252 (1988).

26 Borg, H. J., van den Oetelaar, L. C. A. & Niemantsverdriet, J. W. Preparation of a rhodium catalyst from rhodium trichloride on a flat, conducting alumina support studied with static secondary ion mass spectrometry and monochromatic X-ray photoelectron spectroscopy. *Catal. Lett.* **17**, 81-95 (1993).

27 Grass, M. E. *et al.* A reactive oxide overlayer on rhodium nanoparticles during CO oxidation and its size dependence studied by in situ ambient-pressure X-ray photoelectron spectroscopy. *Angew. Chem. Int. Ed.* **47**, 8893-8896 (2008).

28 Freakley, S. J., Ruiz-Esquius, J. & Morgan, D. J. The X-ray photoelectron spectra of Ir, IrO_2 and $IrCl_3$ revisited. *Surf. Interface Anal.* **49**, 794-799 (2017).

29 Conte, M. *et al.* Hydrochlorination of acetylene using supported bimetallic Au-based catalysts. *J. Catal.* **257**, 190-198 (2008).

30 Sun, X. *et al.* Facile synthesis of precious-metal single-site catalysts using organic solvents. *Nat. Chem.* **12**, 560-567 (2020).

31 Ye, L. *et al.* Self- regeneration of Au/CeO_2 based catalysts with enhanced activity and ultra-stability for acetylene hydrochlorination. *Nat. Commun.* **10**, 914 (2019).

32 Li, G., Li, W. & Zhang, J. Strontium promoted activated carbon-supported gold catalysts for non-mercury catalytic acetylene hydrochlorination. *Catal. Sci. Technol.* **6**, 3230-3237 (2016).

33 Shang, S. *et al.* Highly efficient Ru@IL/AC to substitute mercuric catalyst for acetylene hydrochlorination. *ACS Catal.* **7**, 3510-3520 (2017).

34 Zhang, H. *et al.* Ru-Co(III)-Cu(II)/SAC catalyst for acetylene hydrochlorination. *Appl. Catal. B* **189**, 56-64 (2016).

35 Malta, G., Freakley, S. J., Kondrat, S. A. & Hutchings, G. J. Acetylene hydrochlorination using Au/carbon: a journey towards single site catalysis. *Chem. Commun.* **53**, 11733-11746 (2017).